Journal of Computational Neuroscience
https://doi.org/10.1007/s10827-021-00800-w

ORIGINAL ARTICLE

Dynamics of ramping bursts in a respiratory neuron model

Muhammad U. Abdulla[1] · **Ryan S. Phillips**[2,3] · **Jonathan E. Rubin**[2,3]

Received: 24 April 2021 / Revised: 24 September 2021 / Accepted: 29 September 2021

Abstract
Intensive computational and theoretical work has led to the development of multiple mathematical models for bursting in respiratory neurons in the pre-Bötzinger Complex (pre-BötC) of the mammalian brainstem. Nonetheless, these previous models have not captured the pre-inspiratory ramping aspects of these neurons' activity patterns, in which relatively slow tonic spiking gradually progresses to faster spiking and a full-blown burst, with a corresponding gradual development of an underlying plateau potential. In this work, we show that the incorporation of the dynamics of the extracellular potassium ion concentration into an existing model for pre-BötC neuron bursting, along with some parameter adjustments, suffices to induce this ramping behavior. Using fast-slow decomposition, we show that this activity can be considered as a form of parabolic bursting, but with burst termination at a homoclinic bifurcation rather than as a SNIC bifurcation. We also investigate the parameter-dependence of these solutions and show that the proposed model yields a greater dynamic range of burst frequencies, durations, and duty cycles than those produced by other models in the literature.

Keywords Neuronal dynamics · Fast-slow dynamics · Pre-Bötzinger Complex · Ion concentration dynamics · Persistent sodium current

1 Introduction

Since the original discovery of respiratory activity in neurons within the pre-Bötzinger Complex (pre-BötC) of the mammalian brainstem (Smith et al., 1991), many experimental and computational efforts have focused on characterizing the activity patterns of these neurons. Experiments have shown that, when synaptically isolated, a subset of pre-BötC inspiratory neurons generate temporally clustered action potentials known as bursts (Johnson et al., 1994). These neurons are often referred to as intrinsic bursters or pacemaker neurons. Intrinsic bursting in some pre-BötC neurons has been shown to depend on a persistent sodium current (Butera et al., 1999; Del Negro et al., 2002, 2005; Koizumi & Smith, 2008), while others require a nonspecific cation, or CAN, current (Thoby-Brisson & Ramirez, 2001; Peña et al., 2004), and combinations of these ion flows can produce various distinctive burst patterns including some that may arise under special conditions such as early in development (Jasinski et al., 2013; Chevalier et al., 2016; Wang & Rubin, 2020) or during sighs (Jasinski et al., 2013; Toporikova et al., 2015; Wang et al., 2017).

Functional respiratory rhythms under normoxic conditions consist of three activity phases, commonly known as inspiration, post-inspiration, and late expiration, the latter two of which together comprise expiration. During respiratory rhythms recorded in various experimental preparations, a subpopulation of glutamatergic pre-BötC neurons, sometimes known as type-1 pre-BötC neurons (Rekling & Feldman, 1998; Gray et al., 1999) engages in what is known as pre-inspiratory (pre-I) activity. These neurons remain silent throughout much of post-inspiration and late expiration, but they begin to activate toward the end of the expiration. Their activity ramps in

Communicated by Action Editor: David Terman.

✉ Jonathan E. Rubin
jonrubin@pitt.edu

Muhammad U. Abdulla
muhammadabdulla@ufl.edu

Ryan S. Phillips
ryanp@pitt.edu

[1] Department of Mathematics, University of Florida, Gainesville, FL, USA

[2] Department of Mathematics, University of Pittsburgh, Pittsburgh, PA, USA

[3] Center for the Neural Basis of Cognition, Pittsburgh, PA, USA

intensity, with a gradual increase in the spike rate and in the voltage to which membrane potential repolarizes between spikes as expiration gives way to inspiration, and culminates in bursting that continues throughout inspiration; indeed, this pre-I activity pattern is thought to play an important role in initiating the expiration-to-inspiration transition (Richter, 1996; Ezure et al., 2003; Rubin et al., 2009; Lindsey et al., 2012). While the gradual intensification of pre-I activity likely involves network mechanisms including positive feedback induced by the recruitment of additional neurons, experiments have shown that even individual burst-capable pre-BötC neurons can generate ramping activity patterns, in which tonic spiking eventually intensifies and transitions to bursting, under pharmacological blockade of glutamatergic neurotransmission (Thoby-Brisson & Ramirez, 2001; Peña et al., 2004).

Despite the significant work done previously to model pre-BötC neuronal activity, current spiking models do not capture the ramping activity observed in individual pre-BötC neurons. Moreover, experiments show that the bursting capability of pre-BötC neurons and networks depends on the extracellular ion concentrations to which they are exposed. Slices of 250-350 μm thickness prepared from the pre-BötC are nonrhythmic at physiological $[\mathrm{K}^+]_{\mathrm{ext}}$, but some individual pre-BötC neurons do burst in these conditions (Del Negro et al., 2001; Tryba et al., 2003), especially if depolarized by a tonic input (Smith et al., 1991), and pharmacological blockade of $\mathrm{GABA_A}$ and glycinergic inhibition also allows pre-BötC neurons to burst in these conditions (Tryba et al., 2003). In contrast to these results, modeling that explains how different extracellular potassium concentrations can produce corresponding forms of pre-BötC activity has led to the conclusion that individual pre-BötC neurons should not be able to burst at physiologically relevant extracellular potassium concentrations (Bacak et al., 2016b). In this paper, we revisit these issues, producing and analyzing what is to our knowledge the first Hodgkin-Huxley (HH) style model for ramping bursts of pre-BötC neurons in the absence of rhythmic drive and inhibitory inputs. Importantly, our model does not require tuning outside of physiological parameter ranges in order to produce bursting dynamics.

Many of the previous models that inspired this work were also posed in the HH framework. While neuronal spikes each last just a few milliseconds, inspiratory bursts are much longer events, lasting up to multiple seconds under some experimental conditions (Gray et al., 1999; Thoby-Brisson & Ramirez, 2001; Peña et al., 2004). Despite the presence of ionic pumps and glial cells that regulate intra- and extracellular ion concentrations, respectively, spiking that continues over such prolonged periods can lead to significant changes in the ion concentrations that impact neurons (Fröhlich et al., 2008; Barreto & Cressman, 2011; Kueh et al., 2016). Given this ionic dynamics and the knowledge that pre-BötC respiratory neuron activity patterns strongly depend on extracellular potassium concentration, we hypothesized that the dynamics of potassium ions could be central to the emergence of ramping activity in individual pre-BötC neurons. The key innovation in our work relative to past pre-BötC neuron models is that we have augmented the HH modeling framework with this ionic dynamics. In this paper, we show that combining these components yields a neuronal model that successfully produces ramping dynamics. Applying fast-slow decomposition and associated bifurcation analysis, we explain the mechanisms underlying this activity pattern, which we find represents a form of parabolic bursting. Furthermore, we use direct simulations to explore the robustness and tunability of the bursting dynamics in our model, and we perform additional analysis to elucidate how transitions between bursting and other forms of activity occur as certain model parameters are varied.

2 Model

2.1 Voltage dynamics

We consider a model that depicts the spiking behavior of an isolated neuron in the pre-BötC. It is formulated similarly to other HH-style models (Hodgkin & Huxley, 1952) and depends on a persistent sodium current to trigger bursting (Butera et al., 1999). Our model is based heavily on a model presented by Bacak et al. (2016b), augmented with some crucial modifications.

In this model, the membrane potential (V) is governed by the current balance equation:

$$C \cdot \frac{dV}{dt} = -\left(I_{Na} + I_{NaP} + I_K + I_L + I_{Syn}\right). \tag{1}$$

The membrane currents in (1) include: the fast sodium current I_{Na}, the persistent sodium current I_{NaP}, the delayed rectifier potassium current I_K, the leakage current I_L, and the synaptic current I_{Syn}. These membrane currents are drawn from previous work of Butera et al. (1999) and Bacak et al. (2016b), and are represented as follows:

$$I_{Na} = \bar{g}_{Na} \cdot (m_{Na})^3 \cdot h_{Na} \cdot (V - E_{Na}), \tag{2}$$

$$I_{NaP} = \bar{g}_{NaP} \cdot m_{NaP} \cdot h_{NaP} \cdot (V - E_{Na}), \tag{3}$$

$$I_K = \bar{g}_K \cdot n^4 \cdot (V - E_K), \tag{4}$$

$$I_L = \bar{g}_L \cdot (V - E_L), \tag{5}$$

$$I_{Syn} = \bar{g}_{Syn} \cdot (V - E_{Syn}). \tag{6}$$

Note that we model a single neuron, and I_{Syn} is a tonic synaptic current with time-independent conductance, $\bar{g}_{Syn}$, representing a steady level of drive from other sources, such as brainstem feedback pathways. This form of synaptic current is appropriate for this study, since we are interested in rhythmicity that can emerge due to intrinsic neuronal dynamics, without contributions from time-varying inputs.

2.2 Sodium and potassium currents

The currents I_{Na}, I_{NaP}, and I_K are given as products of maximal conductances, gating variables, and restoring potentials. Each of the sodium gating variables $x \in \{m_{Na}, h_{Na}, m_{NaP}, h_{NaP}\}$ satisfies the equation

$$\tau_x(V) \cdot \frac{dx}{dt} = x_\infty(V) - x, \tag{7}$$

where

$$x_\infty(V) = \left[1 + \exp\left((V_x - V)/k_x\right)\right]^{-1},$$
$$\tau_x(V) = \bar{\tau}_x / \left[\cosh\left((V - V_{\tau_x})/k_{\tau_x}\right)\right].$$

The parameter values used for these equations, with corresponding sources and rationales, are all presented in Appendix 1.

The potassium current only has activation gates, represented by the variable n, which also satisfies Eq. (7). For $n_\infty(V)$ and $\tau_n(V)$, we use the formulation

$$n_\infty(V) = \frac{\kappa_1(V)}{\kappa_1(V) + \kappa_2(V)}, \quad \tau_n(V) = \frac{1}{\kappa_1(V) + \kappa_2(V)},$$

where $\kappa_1(V)$ and $\kappa_2(V)$ are the following voltage-dependent functions, taken from Bacak et al. (2016b) and Huguenard and McCormick (1992):

$$\kappa_1(V) = \frac{n_A \cdot (n_{A_V} + V)}{1 - \exp\left(-(n_{A_V} + V)/n_{A_k}\right)},$$
$$\kappa_2(V) = n_B \cdot \exp\left(-(n_{B_V} + V)/n_{B_k}\right).$$

The constants n_A, n_B, n_{A_V}, n_{B_V}, n_{A_k}, and n_{B_k} are discussed in Appendix 1.

The reversal potential for potassium ions, denoted E_K, is viewed as a function of the dynamic variable $[K^+]_{out}$, and modeled through the Nernst equation approximated at body temperature,

$$E_K = 26.7 \cdot \log \frac{[K^+]_{out}}{[K^+]_{in}}. \tag{8}$$

Note that $[K^+]_{in}$ is taken to be a constant value. The justification for this approximation is discussed in Sect. 2.3. Internal and external sodium ion concentration, and thus also the sodium reversal potential E_{Na}, are taken as constants in this model as in the previous literature (Bacak et al., 2016b), with values listed in Appendix 1.

2.3 Ion regulation and dynamics

The crucial difference between our model and the model presented in Bacak et al. (2016b) is the inclusion of dynamics in the concentration of extracellular potassium ions, denoted $[K^+]_{out}$.

Experimental data has long indicated that neuronal activity causes fluctuations in $[K^+]_{out}$, with increases on the order of 1.0 mM, which can nearly double the $[K^+]_{out}$ local to a neuron, during active periods (Baylor & Nicholls, 1969; Amzica et al., 2002) and increases of up to 10 mM within pathological states such as seizures (Raimondo et al., 2015).

Experimental manipulations that increase the extracellular potassium concentration are commonly performed in *in vitro* studies to increase neural excitability and induce bursting behavior. A typical approach is to bathe slices of neuronal tissue in highly concentrated K^+ solution. The variations of $[K^+]_{out}$ due to neural activity and effects of ion pumps, glia, and diffusion (Clausen et al., 2017; Kofuji & Newman, 2004; Beckner, 2020), however, imply that this bath concentration is not equivalent to what we present as the $[K^+]_{out}$ variable. Throughout this paper, $[K^+]_{out}$ represents the approximate localized concentration of K^+ in the vicinity of an individual neuron, while k_{bath} represents the concentration of potassium in the bathing solution, toward which $[K^+]_{out}$ would naturally evolve over time in the absence of neuronal activity and glial effects. This diffusion of the dynamic $[K^+]_{out}$ variable towards k_{bath} is modeled as a molar current of the form discussed in Barreto and Cressman (2011):

$$\tilde{I}_{diff} = \frac{1}{\tau_{diff}}([K^+]_{out} - k_{bath}), \tag{9}$$

where τ_{diff} represents the corresponding time constant. To simulate reasonable physiological conditions, k_{bath} was set to 4 mM (Barreto & Cressman, 2011).

Glial cells also play an active role in decreasing the concentration of K^+ external to neurons (Newman & Reichenbach, 1996). The effects of the glia on this concentration are also modeled as molar currents in the style of Barreto and Cressman (2011), with maximal rate $\bar{G}$, half-activation potassium concentration $\bar{K}$, and steepness factor z_k as follows:

$$\tilde{I}_{glia} = \frac{\bar{G}}{1 + e^{z_k \cdot (\bar{K} - [K^+]_{out})}}. \tag{10}$$

Note that neither diffusion nor glial cells move ions across the neuronal membrane, and thus the currents $\tilde{I}_{diff}, \tilde{I}_{glia}$ do not appear in the voltage equation.

Finally, increases in $[K^+]_{out}$ are driven by the action potentials of the neuron. The potassium current I_K derives from the movement of potassium ions across the neural membrane. The resulting changes in potassium concentration are therefore proportional to I_K. The proportionality factor is the product of two constants. One of these terms, γ, represents the ratio of the time-derivative of the internal ion concentration to the corresponding membrane current and is derived in Appendix 2. The constant β represents the ratio of the internal neuron volume to the localized external volume, which determines the reversal potential across the neural membrane. Thus, changes in external concentration must be proportional to a factor of $\gamma\beta$ and we model the dynamics of localized external potassium concentration as

$$\frac{d[K^+]_{out}}{dt} = \gamma\beta I_K - \tilde{I}_{diff} - \tilde{I}_{glia}. \tag{11}$$

We note that previous computational models of ion dynamics have set $\beta = 7$ (Barreto & Cressman, 2011). This value can be derived from experimental measurements suggesting that the proportion of total tissue volume that composes extracellular space (ECS) is around 13%. However, studies have found this proportion to range from as low as 4% to a maximum of 24% in conditions of hypoxia or anoxia (Somjen, 2004; Nicholson & Syková, 1998). We used $\beta = 14.555$ in our simulations as we found that that value resulted in a good match to experimental voltage traces (e.g., Fig. 2). Our model produces qualitatively similar dynamics over a wide range of β values as long as τ_{diff} is increased and/or $\bar{G}$ is decreased correspondingly.

Also, it is important to note that in this model, $[K^+]_{in}$ is approximated as being a constant value, despite the fact that K^+ ions inside the neuron flow through the neural membrane via the I_K current and increase $[K^+]_{out}$. The change in external K^+ concentration, which is under 2 mM per burst in this model, would only correlate to a decrease of 0.137 mM in internal K^+ concentration. This is negligible on the scale of bursting behavior of an individual neuron, as it constitutes only a small fraction of the initial $[K^+]_{in}$ value of 150 mM. This approximation was also used in a previous neuronal bursting model with dynamic ion concentrations, based on the argument that changes in $[K^+]_{in}$ are more strongly correlated to fluctuations in internal sodium ion concentration than to changes in $[K^+]_{out}$ (Barreto & Cressman, 2011).

2.4 The full model

In summary, we arrive at a 7-dimensional model of a neuron, which depicts bursting behavior by connecting the dynamics of membrane potential, sodium and potassium gating and reversal potentials, and ion concentrations. The formulations of these dynamics are based on a combination of previous models of bursting behavior (Butera et al., 1999; Bacak et al., 2016b; Barreto & Cressman, 2011). The differential equations in this system are Eqs. (1), (7), and (11); note that in fact we have 5 equations of the form (7), one for each of m_{Na}, h_{Na}, m_{NaP}, h_{NaP}, and n.

2.5 Data analysis and definitions

2.5.1 Ramping bursts

A major aspect of this work is the consideration of ramping bursts, which have not been well captured by other single-neuron conductance-based models. We define ramping bursts as activity patterns with alternating silent and active phases, in which each active phase begins with relatively low frequency tonic spikes, the baseline voltage and the spike frequency gradually rise, forming the ramp, and eventually the dynamics transitions into a period of full-blown high frequency spiking riding on top of a depolarized voltage plateau. The model can produce ramping bursts in two types of parameter regimes: those for which the model with fixed $[K^+]_{out}$ also has a bursting capability (if $[K^+]_{out}$ is fixed in a suitable range) and those for which the model cannot burst for any fixed level of $[K^+]_{out}$. In the former case, we specifically define a ramping burst as a burst where the external potassium ion concentration $[K^+]_{out}$ after the first three spikes is less than the $[K^+]_{out}$ required to induce bursting behavior for the model with the same conductance parameters, but with a fixed external potassium ion concentration.

2.5.2 Fast and slow variables

Our analysis will be based on the premise that $[K^+]_{out}$ and h_{NaP} are the slowest variables in our model. Various methods including nondimensionalization can be used to identify timescales associated with variables in biological models. In our model, such analysis is unnecessary because most of the model equations are of the form (7), with an explicit voltage-dependent timescale term $\tau_x(V)$. It is easy to check directly that $\tau_{h_{NaP}}(V)$ is at least 10 times larger than all of the other timescale terms for each V in the range occurring in our simulations. Moreover, direct simulation shows that the rate of change of $[K^+]_{out}$ is also slow relative to the rates of change of these other terms and voltage (e.g., see Fig. 2). At a more analytical level, we note that the key term controlling the magnitude of the rate of change of $[K^+]_{out}$ is I_K, which includes the quantity n^4. In theory, n^4 could become as large as 1, which would increase the magnitude of I_K and speed up the change of $[K^+]_{out}$. In our simulations, however, n remains below a maximum of around 0.5. With this constraint, the quantity $|d[K^+]_{out}/dt|/(\Delta K)$, where ΔK denotes the range of values over which $[K^+]_{out}$ varies (Diekman et al., 2017), stays small relative to comparable quantities for voltage and the gating variables other than h_{NaP}.

3 Periodic behaviors in the model

3.1 Activity patterns

To match experimental data, a pre-BötC neuron model must demonstrate a range of activity patterns across different conditions. Previous modeling work showed how different neuronal behaviors occur at different fixed values of the external potassium concentration, and our model reproduces this result in Fig. 1. Specifically, at sufficiently negative E_K, the neuron remains in a tonic spiking state, characterized by rhythmic spiking at a fixed frequency (Fig. 1A). As E_K is increased, bursting dynamics, with periods of quiescence alternating with periods of high-frequency spiking riding a depolarized voltage plateau, emerges (Fig. 1B). With even higher E_K, however, after release from the original resting potential, the neuron spikes but cannot fully repolarize and return to a resting state and instead, it again enters a tonic spiking state but with reduced repolarization and a higher frequency (Fig. 1C). Finally, when E_K is high enough, the neuron enters depolarization block with an elevated membrane potential and no spike generation (Fig. 1D). The agreement of these simulations with previous work is not surprising: When internal and external K^+ concentrations are fixed, our model is extremely similar to the model presented in Bacak et al. (2016b), differing only in the values of a few model parameters, which affect quantitative but not qualitative aspects of the dynamics in this frozen-potassium setting.

Previous work has noted that fixing $[K^+]_{out}$, which is directly related to E_K by (8), at values sufficiently elevated above physiological levels is enough to induce bursting in a pre-BötC neuron model lacking ion concentration dynamics (Bacak et al., 2016b). Furthermore, modeling of other brain areas revealed a wide array of bursting behaviors when K^+ and Na^+ concentrations were allowed to vary dynamically (Barreto & Cressman, 2011; Erhardt et al., 2020). In this work, we combine the insights offered by these earlier investigations to model pre-BötC dynamics featuring ramping activity culminating in a burst without imposed elevation of extracellular potassium concentration.

Indeed, with dynamic extracellular potassium levels, our model produces distinctive ramping bursts as shown in Fig. 2, matching a pattern seen experimentally in pre-BötC neurons; the slow spiking on a gradually increasing voltage plateau at the start of each burst active phase is referred to in the literature as "pre-inspiratory activity". These bursts include periods of quiescence, during which $[K^+]_{out}$ remains on the low end of physiologically observed levels, corresponding to low values of E_K, by Eq. (8). Numerical simulations show that E_K slowly increases during this phase until spiking emerges. As in other HH-type models, each spike

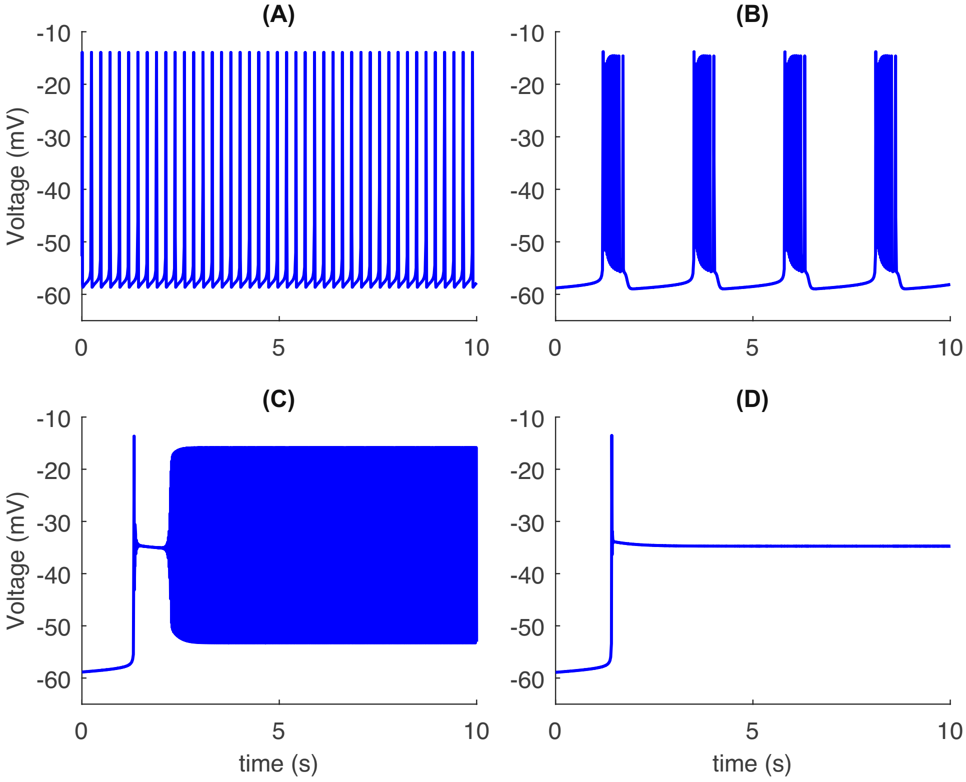

Fig. 1 Model pre-BötC neuron activity depends on the potassium reversal potential, E_K, which relates to the local external potassium concentration via Eq. (8). **(A)** $[K^+]_{out} = 4.0$ mM, $E_K = -96.8$ mV: low rate tonic spiking. **(B)** $[K^+]_{out} = 6.0$ mM, $E_K = -85.9$ mV: bursting. **(C)** $[K^+]_{out} = 8.0$ mM, $E_K = -78.3$ mV: transient followed by high rate tonic spiking. **(D)** $[K^+]_{out} = 10.0$ mM, $E_K = -72.3$: depolarization block

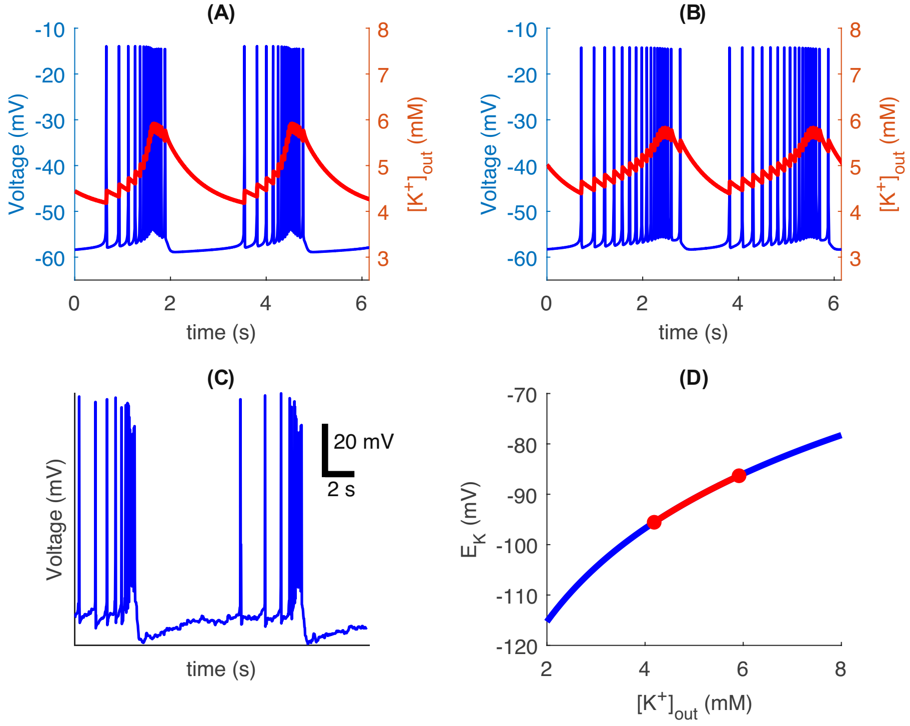

Fig. 2 Typical bursting trajectories of our pre-inspiratory pre-BötC neuron model. (**A**) Time course and external potassium concentration for $\bar{g}_{NaP} = 5.0$ nS, $\bar{g}_L = 2.50$ nS, $\bar{g}_{Syn} = 0.365$ nS. (**B**) Time course and external potassium concentration for $\bar{g}_{NaP} = 4.5$ nS, $\bar{g}_L = 2.40$ nS, $\bar{g}_{Syn} = 0.360$ nS. (**C**) Physiologically recorded ramping behavior, adapted with publisher's permission from Fig. 4 in Gray et al. (1999). (**D**) Monotonic relationship between external potassium ion concentration and potassium reversal potential, with range from (**A**, **B**) indicated in red

involves dynamics of the sodium and potassium currents, I_{Na} and I_K, respectively. The ion flows associated with these currents gradually increase $[K^+]_{out}$. Although glia and diffusion also contribute to changes in external K^+ concentrations, the strengths of these repolarization currents depend on $[K^+]_{out}$ as depicted in Eqs. (9) and (10). Moreover, at low concentrations, we find that the glia are almost inactive and diffusion is too weak to bring $[K^+]_{out}$ back to equilibrium. A positive feedback loop results, with neuronal spiking causing $[K^+]_{out}$ to increase and increases in $[K^+]_{out}$ driving intensification of spiking, such that $[K^+]_{out}$ rises substantially above baseline values. Our simulations show that this rise in $[K^+]_{out}$ is cut off by the rise in the strength of diffusion and glial currents as in Eqs. (9) and (10). The overall increase of E_K is enough to trigger bursting behavior in the neural cell, however, and this bursting continues until some time after $[K^+]_{out}$ saturates. Furthermore, as demonstrated experimentally (Del Negro et al., 2001) and discussed near the end of Sect. 3.2, the spiking frequency increases with $[K^+]_{out}$. Thus, the increasing $[K^+]_{out}$ during the build-up of a burst also provides a mechanism for a *ramping effect*, where the spiking frequency gradually increases from an initial slow tonic spiking until a burst is established. The exact geometry of the burst pattern depends on various parameters, including maximal conductance strengths. For example, with a reduction in $\bar{g}_{NaP}$, $\bar{g}_L$, and $\bar{g}_{Syn}$ the bursting pattern changes to feature a more gradual increase in spike frequency and a less pronounced drop in spike amplitude during the burst (Fig. 2B). As noted in Sect. 2.4, this second parameter set corresponds to a regime in which the model can never burst with $[K^+]_{out}$ fixed. This distinction will also show up in the analysis in the coming sections.

3.2 Fast-slow decomposition analysis

Neuronal bursting results from dynamics occurring across two or more distinct timescales. Voltage spikes occur on a fast timescale. Transitions between the spiking state and quiescent state within the bursting regime, as well as the gradual oscillation of $[K^+]_{out}$ over the course of a burst, depend on slow timescale dynamics. In our model, a positive feedback loop between the slow subsystem and the fast subsystem causes a buildup in external K^+ concentration and a gradual increase in spike frequency during the active phase of a burst. The resulting variation in E_K values affects the timing of the transition from the active spiking state to the quiescent state within each burst.

A fast-slow decomposition is a standard mathematical approach to elucidate the details of multiple timescale dynamics in bursting (Bertram & Rubin, 2017). We begin a fast-slow decomposition by noting that h_{NaP} and $[K^+]_{out}$ evolve significantly more slowly that the other variables in the model. Hence, the full model can be considered as having 5 fast variables $(V, m_{Na}, h_{Na}, n, m_{NaP})$, comprising a fast subsystem, and 2 slow variables h_{NaP} and $[K^+]_{out}$, constituting a slow subsystem.

A standard approach when a model features multiple slow variables, which we follow, is to pick one of these as a primary bifurcation parameter and compute bifurcation diagrams for the fast subsystem with respect to this parameter, while the other slow variables are held frozen at some fixed values. This process can then be repeated for various values of these other slow variables, which are typically selected based on the paths they follow when the full system evolves.

Previous analysis of respiratory neuron models with fixed E_K showed the utility of h_{NaP} as a bifurcation parameter (Butera et al., 1999; Bacak et al., 2016b), so we make h_{NaP} our initial primary bifurcation parameter as well, and we use XPPAUT (Ermentrout, 2002) to consider how the dynamics of the fast subsystem varies with h_{NaP}. We repeat this analysis for several values of $[K^+]_{out}$ (and hence of E_K). Note that we refer to the fast subsystem together with h_{NaP} as the *neuronal system*.

Let us start with the parameter set corresponding to Fig. 2A. Consider first $[K^+]_{out} = 4.5$ mM (Fig. 3A). The fast subsystem bifurcation diagram with respect to h_{NaP} includes an S-shaped curve of equilibria, known as the critical manifold $\mathcal{S}$, including two stable segments (red solid), one a hyperpolarized branch corresponding to quiescence and the other a depolarized segment corresponding to depolarization block. The lower stable branch ends in a saddle-node bifurcation that we call the lower knee of $\mathcal{S}$, with $h = h_{NaP}^{LK}$, while the upper segment destabilizes at even larger h_{NaP} at a supercritical Andronov-Hopf (AH) bifurcation, with $h = h_{NaP}^{AH}$. These bifurcation values do depend on $[K^+]_{out}$, but we suppress this dependence in our notation. The family of stable periodic orbits, $\mathcal{P}$, born in the AH bifurcation continues for decreasing h_{NaP} until terminating in a SNIC bifurcation at the lower knee. When the neuronal system, consisting of the fast subsystem along with the slow h_{NaP} dynamics, is simulated with $[K^+]_{out}$, and thus E_K, still frozen, the system exhibits periodic tonic spiking in which h_{NaP} hovers near a particular value and the voltage of the cell oscillates along the associated part of the periodic orbit family in the bifurcation diagram. Past work has shown that this tonic spiking results when the weak leftward drift in h_{NaP} during the part of each oscillation when the trajectory lies above the h_{NaP}-nullcline (dashed orange) in (h_{NaP}, V)-space exactly balances the weak rightward drift when the trajectory is below the h_{NaP}-nullcline (Bacak et al., 2016b).

When $[K^+]_{out}$ is fixed at the larger value of 5.3 mM, the fast subsystem bifurcation diagram remains similar but the termination of the periodic orbit family decouples from the saddle-node bifurcation; that is, the termination now occurs at a homoclinic bifurcation, with $h = h_{NaP}^{HC}$, instead of at a SNIC. The shift in the periodic orbit family due to the selection of a new E_K value also changes its relation to the position of the h_{NaP}-nullcline and its shape. As a result, the trajectory of the neuronal system drifts in the direction of lower h_{NaP} as spiking occurs until it reaches the h_{NaP} value of the homoclinic bifurcation and returns to the silent, non-spiking phase. Thus, this system produces

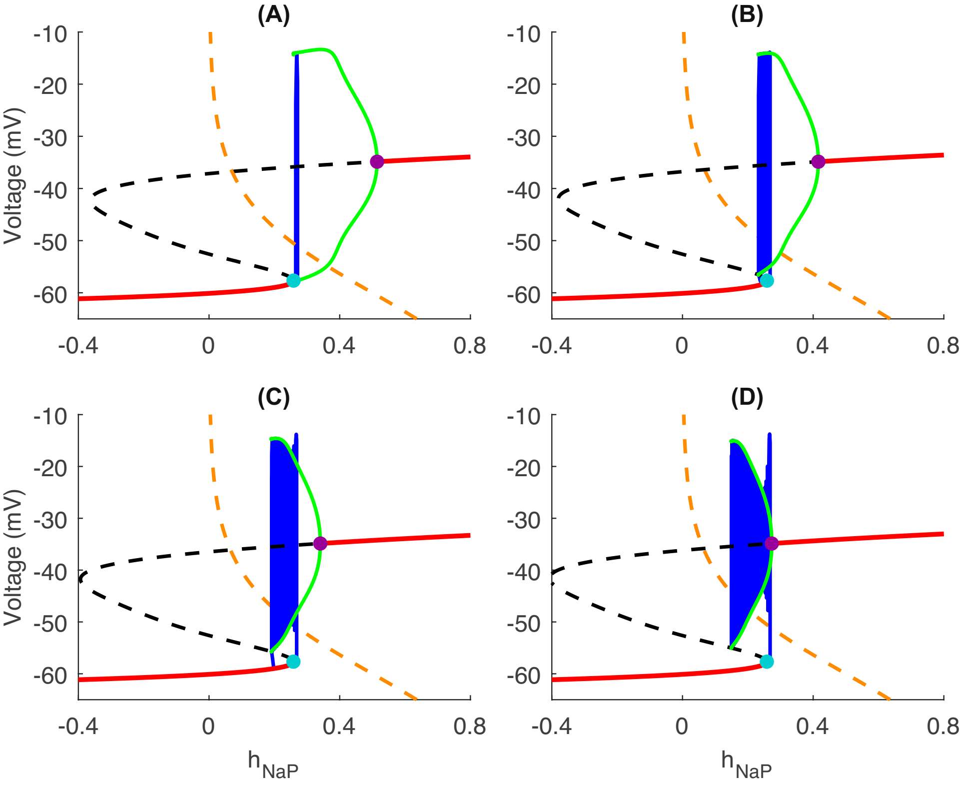

Fig. 3 Both spiking and bursting states can be realized with fixed K^+ concentration (cf. Bacak et al., 2016b). Solid red (dashed black) curves: stable (unstable) segments of the critical manifold; solid purple circle: Andronov-Hopf (AH) bifurcation point; green curve: periodic orbit family $\mathcal{P}$; blue curve: orbit of the neuronal system starting from a jump up to the active phase; dashed orange curve: h_{NaP} nullcline. (**A**) $[K^+]_{out} = 4.5$ mM, $E_K = -93.6$ mV: spiking oscillation near SNIC (light blue) where $\mathcal{P}$ terminates. (**B**) $[K^+]_{out} = 5.3$ mM, $E_K = -89.3$ mV: bursting. (**C**) $[K^+]_{out} = 6.0$ mM, $E_K = -85.9$ mV: bursting with an altered waveform. (**D**) $[K^+]_{out} = 6.7$ mM, $E_K = -83.0$ mV: tonic spiking (note the absence of a jump down in the orbit from $\mathcal{P}$ to the lower stable branch of $\mathcal{S}$; also see main text)

square-wave bursting, also known as fold-homoclinic bursting (Izhikevich, 2007) (Fig. 3B).

As we consider progressively larger (less hyperpolarized) values of $[K^+]_{out}$, we find that $\mathcal{P}$, h_{NaP}^{AH}, and h_{NaP}^{HC} all move to smaller h_{NaP} values. Moreover, the curve of maximal voltages along the periodic orbit family continues to change shape, becoming monotone decreasing in h_{NaP} instead of non-monotonic as previously. When $[K^+]_{out} = 6.0$ mM, for example, the neuronal system continues to produce bursting dynamics, but with bursts of longer duration and more spikes per burst than previously (Fig. 3C). As h_{NaP}^{AH} becomes closer to h_{NaP}^{SN}, the initial spikes within each burst have a large amplitude but subsequent spikes are smaller, as the orbit converges down to small-amplitude fast subsystem periodic orbits near the AH point; as time continues to evolve, spikes become larger again, as the bursting orbit travels toward the homoclinic, where the fast subsystem periodics have larger amplitude. This decreasing-increasing trend in spike amplitudes becomes more pronounced as $[K^+]_{out}$ increases and h_{NaP}^{AH} moves to successively smaller h_{NaP}.

Finally, at a $[K^+]_{out}$ value above a certain threshold, the neuronal system no longer produces bursting behavior. For example, for $[K^+]_{out} = 6.7$ mM, the AH point now lies to the left of the saddle-node point. Hence, if we start a trajectory in the silent phase, then after h_{NaP} grows and reaches the SN point to initiate spiking, the initial decline in spike amplitude is particularly pronounced, as the trajectory initially converges toward the depolarized branch of fast subsystem equilibria (Fig. 3D). Furthermore, thanks to the more extreme leftward position of the periodic orbit family, the spikes that occur at low h_{NaP} spend significant time below the h_{NaP}-nullcline in the (h_{NaP}, V) plane, allowing the corresponding rightward drift in h_{NaP} to balance the leftward drift that occurs when voltage is more depolarized. Thus, the trajectory becomes pinned and oscillates along a particular fast subsystem periodic orbit indefinitely, as it did for $[K^+]_{out} = 4$ mM, and the neuron remains in a tonic spiking state.

Next, consider the parameter set with $\bar{g}_{Syn} = 0.360$ nS, $\bar{g}_{NaP} = 4.5$ nS, and $\bar{g}_L = 2.4$ nS. This reduction in $\bar{g}_L$ is analogous to increasing the excitability of the neuron, as discussed in more detail in Sect. 4. In Fig. 2B, the bursting waveform resulting from this parameter set is demonstrated. However, if $[K^+]_{out}$ is set to be constant, bifurcation analysis with respect to h_{NaP} shows that the neuronal system is unable to achieve a bursting state at any fixed ion concentration, but rather maintains tonic spiking. In this case, with dynamic $[K^+]_{out}$, the gradual rise of $[K^+]_{out}$ essentially drags the trajectory of the neuron along the family of stable limit cycles in the direction of lower h_{NaP}. As these states correspond to higher spiking frequencies, the dynamics of $[K^+]_{out}$ provides a mechanism for an active phase geometry that features a gradual increase in spiking frequency. Thus, we have shown that even a neuron that can never burst on its own with fixed $[K^+]_{out}$ can nonetheless become intrinsically bursting when $[K^+]_{out}$ dynamics are taken into account.

In Appendix 3, we consider in more detail the changes in stable periodic behavior that occur with E_K as a bifurcation parameter.

3.3 Dynamics in (V, h_{NaP}, E_K) phase space

Next, we incorporate the dynamics of E_K back into the picture. Because there are two slow variables, $(h_{NaP}, [K^+]_{out})$, we can follow bifurcations of the fast subsystem in the two-parameter $(h_{NaP}, [K^+]_{out})$ space. Projecting full model trajectories onto this space reveals which bifurcation crossings occur during bursting dynamics, which is crucial for comparing these bursts to known bursting types in the literature (e.g., Izhikevich, 2007). In fact, we find a better visualization if we replace $[K^+]_{out}$ by E_K, a monotone increasing function of $[K^+]_{out}$ as depicted in Fig. 2D. Hence, we consider the trajectory of the full model system projected into the (h_{NaP}, E_K) plane (Fig. 4, blue curves), where it progresses in a counterclockwise fashion. First focus on the parameter set from Fig. 2A; see Fig. 4A. Starting from the quiescent state (the leftmost intersection of the blue neuronal trajectory and the lower purple line), h_{NaP} increases until the trajectory crosses the lower fold of $\mathcal{S}$, the fast subsystem critical manifold (Fig. 4A, black line), which also corresponds to a the termination of the fast subsystem periodic orbit family (Fig. 4A, green curve). If E_K were frozen, then this crossing would result in tonic spiking. Instead, E_K increases as spiking continues. Eventually E_K crosses the value where the neuronal dynamics supports bursting (Fig. 4A, lower purple line). Interestingly, we see that very close to this E_K, the periodic orbit termination curve diverges from the fold line, confirming that the switch from spiking to bursting in the E_K-frozen system corresponds to a switch from termination of the periodic family in a SNIC bifurcation to termination in a homoclinic bifurcation. As E_K continues to increase, the trajectory moves away from the homoclinic curve and towards the AH curve (Fig. 4A, red line with dots). Oscillation amplitude shrinks to zero at an AH bifurcation. Correspondingly, the approach of the trajectory towards the AH curve yields the decrease in spike height seen in Fig. 2A (see also Fig. 9), representing a less extreme form of the amplitude modulation in the burst patterns arising with E_K fixed between −96 and −90 mV (Fig. 3) and in bursting associated with the CAN current in past work (Rubin et al., 2009; Dunmyre et al., 2011; Wang & Rubin, 2016, 2020). Eventually, E_K peaks and then decays slightly due to I_{glia} and I_{diff}, and the decrease in h_{NaP} pulls the trajectory back across the periodic orbit termination curve, terminating the active phase of the burst. A similar

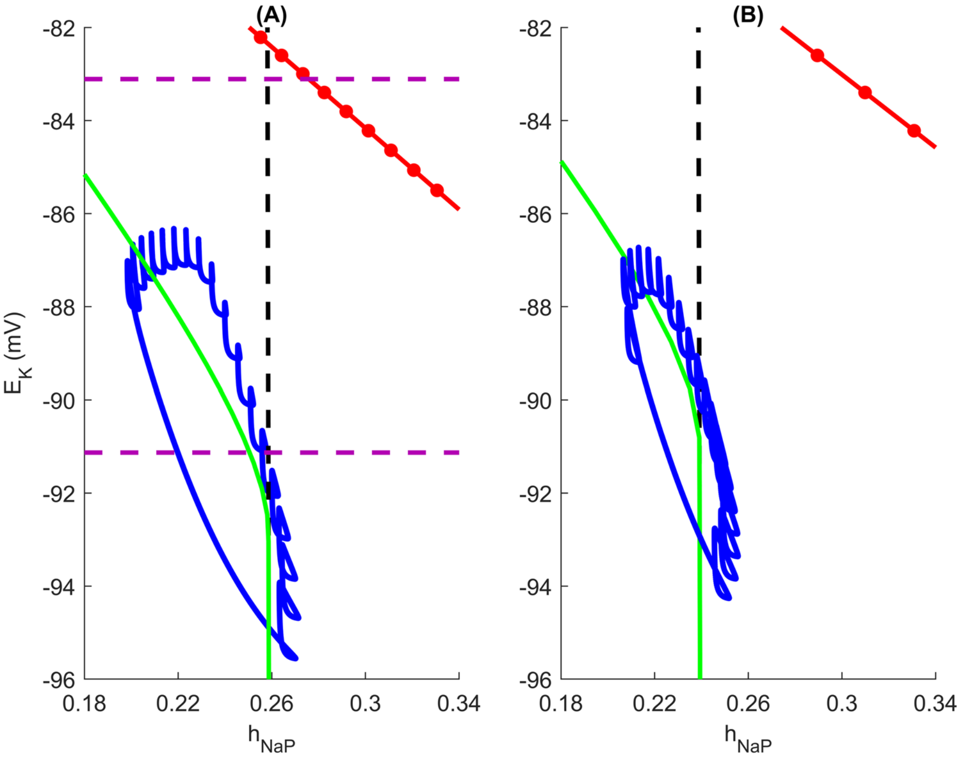

Fig. 4 Projection of the full system bursting trajectory (blue) to the (E_K, h_{NaP}) plane for parameters from (**A**) Fig. 2A ($\bar{g}_{NaP} = 5.0$ nS, $\bar{g}_L = 2.5$ nS, $\bar{g}_{Syn} = 0.365$ nS) and (**B**) Fig. 1B ($\bar{g}_{NaP} = 4.5$ nS, $\bar{g}_L = 2.4$ nS, $\bar{g}_{Syn} = 0.360$ nS). Black dashed lines: fast subsystem fold points; solid-dotted red: fast subsystem AH points; green: fast subsystem periodic orbit termination curve; purple dashed: transitions from spiking to bursting (lower) and bursting to spiking (upper) as E_K is increased; blue: projected model trajectories

picture results from the parameter set from Fig. 2B, as shown in Fig. 4B. There is no purple line here, because the fast subsystem cannot burst for fixed E_K, but a qualitatively identical transition from a SNIC to a homoclinic bifurcation occurs.

Putting everything together, we see that the full model system with dynamic E_K engages in a form of parabolic bursting (Ermentrout & Kopell, 1986; Rinzel, 1987). Parabolic bursting was originally identified as a form of bursting in which the evolution of two slow variables switches the fast subsystem back and forth across a SNIC curve twice per cycle, yielding an alternation between a quiescent regime corresponding to each inter-burst interval and a spiking regime corresponding to the active phase of each burst. This form of bursting was dubbed parabolic in reference to the parabolic shape of the curve depicting spike frequency versus time within each burst, resulting from the low frequency spiking associated with passage near a SNIC bifurcation. In our case, the use of projection shows that the initial slow spiking at the start of the burst active phase corresponds to the slow tonic spiking seen with very hyperpolarized E_K (Fig. 1A), which emerges as the trajectory evolves near the fast subsystem SNIC bifurcation curve when E_K is low. Interestingly, the transition from a SNIC to a homoclinic bifurcation curve here differs from classical parabolic bursting and accounts for the spike acceleration within the burst and the lack of the significant slowing at the end of the burst typically seen (Fig. 2), consistent with other recent work emphasizing the quantitative variability that can occur within individual bursting classes (Rubin et al., 2018). Appendix 4 provides one more perspective that confirms the nature of the bursting dynamics, namely a visualization of the bursting trajectory in the (E_K, V, h_{NaP}) phase space.

To summarize this whole section, our model utilizes persistent sodium currents (Butera et al., 1999) and dynamic ion concentrations (Barreto & Cressman, 2011) to recreate the ramping pre-inspiratory / inspiratory behavior seen in bursting pre-BötC neurons. Our model is built from a model proposed in previous work (Bacak et al., 2016b), with the addition of dynamic ion concentrations and neuronal regulators (Barreto & Cressman, 2011). The process of bursting in our model can be understood to be a form of parabolic bursting based on two-dimensional projections, fast-slow decomposition and computation of bifurcation curves, and can be visualized fully by graphing in the (E_K, V, h_{NaP}) phase space. Ramping of spike frequency at burst onset depends on the passage of the bursting trajectory near a curve of SNIC bifurcations that terminates a family of fast subsystem periodic orbits and its subsequent departure from this curve, which prevents a symmetric spike deceleration at the end of each burst. This burst mechanism does not require there to be a fixed value of E_K at which the remaining equations produce bursting (Figs. 2B, Fig. 4B). The change in spike heights during the burst depends on how the trajectory travels relative to the AH bifurcation curve that gives rise to the periodic orbits.

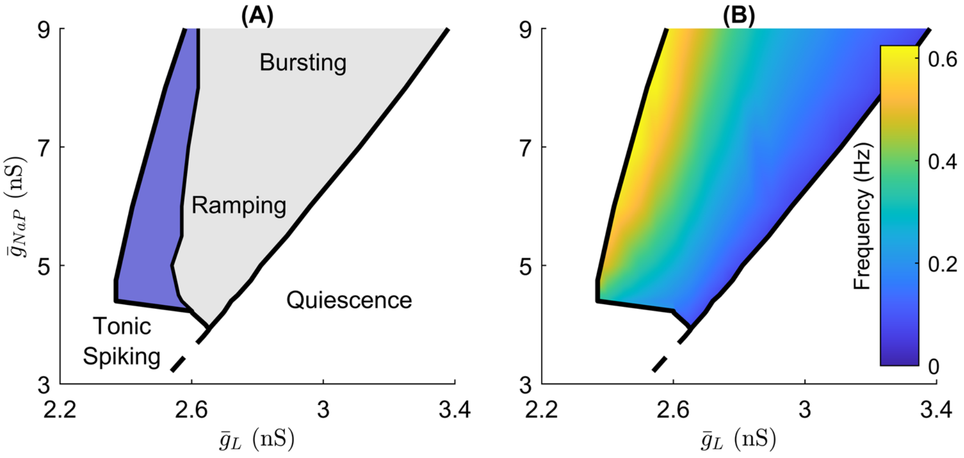

Fig. 5 Bursting within the $(\bar{g}_L, \bar{g}_{NaP})$ parameter space. (**A**) The gray region depicts the set of parameters for which bursting occurs. Within this region, a smaller set of parameters (blue), associated with relatively low $\bar{g}_L$ values, correspond to ramping bursts. Parameter sets with lower $\bar{g}_L$ than in the bursting region correspond to tonic spiking behavior, while higher $\bar{g}_L$ leads to quiescence. (**B**) The burst frequencies for parameter values within the bursting region are indicated by the gradient bar, with more yellow regions corresponding to greater frequencies

4 Robustness of model dynamics

4.1 Robustness in maximal conductance parameters

A critical question for any model in which the details of an activity pattern are important is robustness to variation in parameters. Experimental results have confirmed that the presence of persistent sodium (I_{NaP}) and leakage (I_L) currents are essential to pacemaker activity in pre-BötC neurons (Del Negro et al., 2002; Koizumi et al., 2010). Thus, we mapped the behavior of the model in the $(\bar{g}_L, \bar{g}_{NaP})$ parameter space to measure the robustness of bursting within the neuron under variation of these parameters (Fig. 5A). While bursting behavior could be achieved over a wide range of physiologically relevant parameter values, ramping bursts were restricted to a smaller parameter set. Furthermore, we also measured bursting frequency within the bursting parameter region (Fig. 5B), demonstrating how the properties of the model bursting patterns are modulated by these maximal conductance levels.

The parameters that induced bursting behavior were also strongly affected by the synaptic input into the neuron. In this model, this tonic input is represented by the current I_{Syn}. The effects of altering synaptic input through variation of $\bar{g}_{Syn}$ on the bursting region within the $(\bar{g}_L, \bar{g}_{NaP})$ parameter space are depicted in Fig. 6. The overall shape of these bursting regions is consistent with previous studies (Del Negro et al., 2002; Purvis et al., 2007), which indicate that pacemaker properties are tied to the $\bar{g}_{NaP}/\bar{g}_L$ ratio. Consistent with this observation, the upper and lower boundaries of the bursting region for our model are approximately linear within the $(\bar{g}_L, \bar{g}_{NaP})$ parameter space.

4.2 Inter-model robustness comparison

To further analyze the effectiveness of the model introduced in this work, its robustness was compared to two existing models of bursting in pre-BötC neurons. Specifically, we examined two facets of robustness: (1) robustness in parameters, i.e., the ability of the model to maintain bursting behavior over a wide range of physiologically observed parameter values, and (2) robustness in behavior modulation, i.e., the ability of the model to demonstrate realistic variation in properties of its activity pattern (including bursting

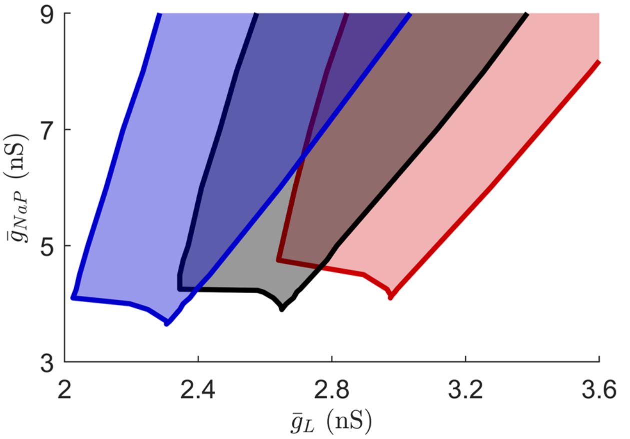

Fig. 6 Bursting behavior can occur over a wide range of $\bar{g}_{NaP}$ and $\bar{g}_L$ values. The bursting region in this parameter space depends on $\bar{g}_{Syn}$. The black region shows the bursting region with the default value $\bar{g}_{Syn} = 0.365$ nS. The blue and red regions show where bursting occurs for lowered ($\bar{g}_{Syn} = 0.300$ nS) and elevated ($\bar{g}_{Syn} = 0.430$ nS) maximal conductances, respectively

frequency, duration, and duty cycle) as parameter values are varied.

First, the new model was compared to the model formulated by Bacak et al. (2016b); structurally, the two models differ only in the fact that our model includes the dynamics of the external potassium ion concentration. Thus, this comparison demonstrates how the introduction of a dynamic ion concentration, which allows for ramping bursts to occur, affects overall robustness. Next, the new model was compared to the model introduced in Butera et al. (1999), which has been incorporated into multiple subsequent computational studies. In the original paper, bursting was induced by increasing E_L, which increased activation in the neuron. To maintain consistency with the general literature, however, we keep E_L fixed and gradually decrease $\bar{g}_L$ to increase activation, and we examine robustness within the $(\bar{g}_L, \bar{g}_{NaP})$ parameter space.

The variation of burst properties (frequency, duration, and duty cycle) under changes in $\bar{g}_L$ is depicted for all three models in Fig. 7. For each model, this variation was tested for reduced, default, and elevated $\bar{g}_{NaP}$ values. To adjust for differences between the models, maximal conductance values were normalized with respect to membrane capacitance. Both our new model and the model from Bacak et al. (2016b) utilize a membrane capacitance of 36 pF, while the model from Butera et al. (1999) utilizes a capacitance of 21 pF. Thus, while the default $\bar{g}_{NaP}$ value in the proposed model is 5.0 nS, assuming constant conductance/capacitance density, the default $\bar{g}_{NaP}$ value in the model in Butera et al. (1999) would be 2.92 nS.

The first thing to note from this analysis is that compared to the model in Bacak et al. (2016b), the new model exhibits its bursting behavior over an almost identical set of $\bar{g}_L$ values for the fixed $\bar{g}_{NaP}$ values tested (Fig. 7A,B). Thus, the introduction of a dynamic ion concentration did not alter the robustness of bursting with respect to the $(\bar{g}_L, \bar{g}_{NaP})$ parameter space. The inclusion of a dynamic ion concentration significantly increased the set of frequency values attainable through variation of $\bar{g}_L$, however. While the model presented in Bacak et al. (2016b) could not reach bursting frequencies above 0.4 Hz, our dynamic potassium model attained bursting frequencies up to 0.6 Hz. It is important to

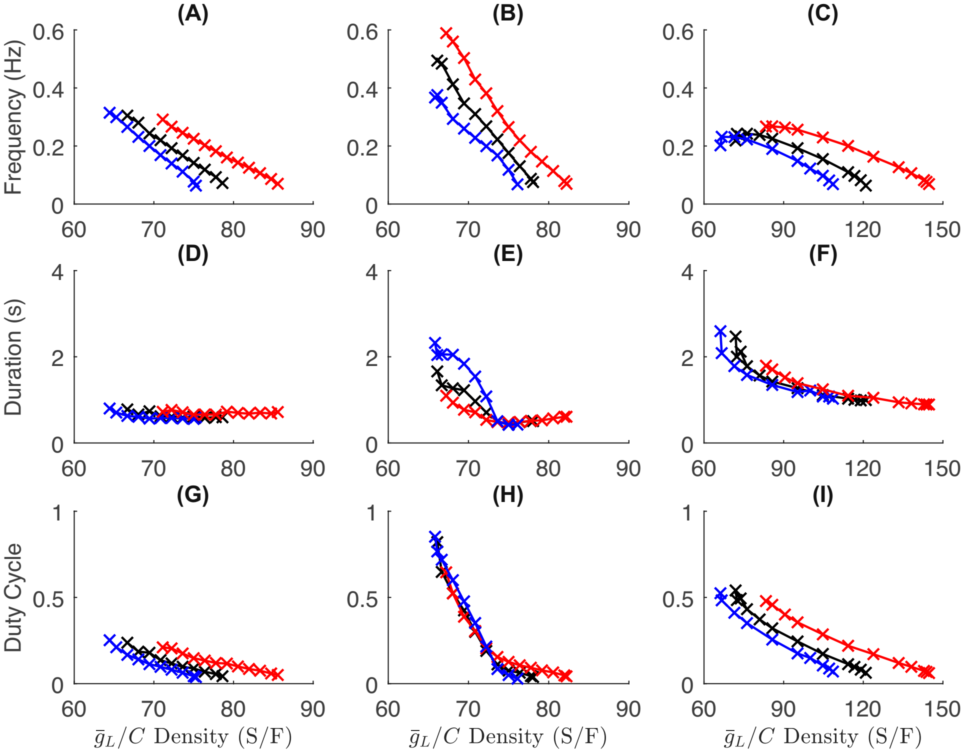

Fig. 7 The effects of $\bar{g}_L$ and $\bar{g}_{NaP}$ on the quantitative characteristics of bursting dynamics compared across different models. The left (**A, D, G**), central (**B, E, H**), and right columns (**C, F, I**) represent the Bacak et al. (2016b) model, the model introduced in this paper, and the Butera et al. (1999) model, respectively. The top row (**A, B, C**), central row (**D, E, F**), and bottom row **G, H, I** show modulation of frequency, burst duration, and burst duty cycle. In all panels: blue, black, and red curves correlate to experiments with reduced, default, and elevated $\bar{g}_{NaP}$ values. In (**A, B, D, E, G, H**) these are 4.5, 5.0, and 6.0 nS. In **C, F, I** these are 2.625, 2.917, and 3.500 nS. The leakage reversals (E_L) for the Bacak et al. (2016b), proposed, and Butera et al. (1999) models were fixed accordingly at −64, −68, and −62 mV. It should be noted that higher bursting frequencies in the Butera et al. (1999) model could be reached by increasing E_L, but this strays further from the experimental value of -68 ± 3.4 mV (Koizumi et al., 2010)

note that, as depicted in Fig. 5, the higher frequency bursts correspond very closely with the newly attainable ramping state. Moreover, the previous model (Bacak et al., 2016b) maintained an essentially constant burst duration under variation of both $\bar{g}_L$ and $\bar{g}_{NaP}$, whereas our model could achieve substantially longer bursts at the low end of the bursting range of $\bar{g}_L$ (Fig. 7D,E). It can be concluded that compared to the static ion concentration model in Bacak et al. (2016b), our proposed model allows for greater modulation of bursting properties through the inclusion of the ramping state, without any significant cost to robustness with respect to maximal conductance parameters.

Compared to the model proposed in Butera et al. (1999), the new model had decreased robustness of bursting with respect to $\bar{g}_L/C$ density, as depicted in Fig. 7B,C. Despite the decrease in this measure of robustness, the new model achieves an increased range of burst frequencies compared to the model proposed in Butera et al. (1999), as shown in Fig. 7B,C. Higher frequency bursts were attainable in the model from Butera et al. (1999), but only with a shift away from physiologically relevant parameters. Our model also achieved a wider range of burst durations than could be produced by the earlier model (Butera et al., 1999) (Fig. 7E, F); specifically, our model allowed for shorter bursts at high $\bar{g}_{NaP}$. Consistent with previous experimental results (Koizumi et al., 2010), the bursting frequency decreased linearly with an increase in $\bar{g}_L$ for all models.

The quality that stood out most about the newly introduced model was the significant increase in the range of possible duty cycles when compared to other models, as shown in Fig. 7G,H,I. The spiking region could be set to account for an extremely low or extremely high percentage of each burst cycle duration spent in the active phase, based on variation of $\bar{g}_L$, for all levels of $\bar{g}_{NaP}$. This flexibility was not possible in the alternative models. Our model produced bursts with large duty cycles in the ramping regime, with relatively low $\bar{g}_L$, with relatively longer, lower frequency bursts for smaller $\bar{g}_{NaP}$ and shorter, faster bursts for larger $\bar{g}_{NaP}$. Neither of the other models could achieve this duty cycle. Our model produced shorter duty cycles for larger $\bar{g}_L$, again for all $\bar{g}_{NaP}$, due to a decrease in burst frequency without much change in burst duration, similar to the other models.

5 Discussion

In this study, we present a model developed from previous conductance-based neuron models that exhibit bursting behavior dependent on a persistent sodium current (Butera et al., 1999; Bacak et al., 2016b). Our model replicates the observed frequency ramping behavior of pre-BötC neurons, through the inclusion of external potassium ion $\left([K^+]_{out}\right)$ dynamics. Previous studies have indicated the relationship between fixed levels of $[K^+]_{out}$ and burst frequency and duration (Del Negro et al., 2001). The incorporation of $[K^+]_{out}$ dynamics as an additional slow component of the model induced a modulation of spike frequency throughout the spiking regime, resulting in a robust parabolic bursting behavior.

The dynamics of the model was analyzed through a three-dimensional extension of the traditional fast-slow decomposition. Steady-state behavior was plotted in the $\left(V, h_{NaP}\right)$-phase space for various fixed values of $[K^+]_{out}$, and hence of E_K as computed via Eq. (8). The curves of saddle-node and AH bifurcations and the families of periodic orbits originating from the AH points were mapped with respect to E_K. These quantities were then projected onto the $\left(E_K, V, h_{NaP}\right)$-phase space, depicting the geometry that ultimately dictates bursting dynamics. While this approach does not capture certain transitional solution patterns that involve subtle interactions of multiple slow variables or mixing of time scales (Vo et al., 2014; Teka et al., 2012; Wang & Rubin, 2016, 2020; Wang et al., 2017; Bertram & Rubin, 2017), it turned out to be an effective way to explain the activity patterns in our simulations. Specifically, tracking the trajectory of the burst through this phase space revealed that oscillations in the $\left(V, h_{NaP}\right)$-phase space gradually drive the trajectory to higher values of E_K; subsequently, higher E_K values correspond to higher frequency spiking, causing a positive feedback loop resulting in ramping bursts. Eventually, the E_K level saturates due to the nonlinear dependence of processing of potassium ions by glia, at which point the slow inactivation of I_{NaP} can terminate the burst. Specifically, as h_{NaP} decays, the fast subsystem periodic orbit family terminates in a homoclinic bifurcation and the voltage repolarizes, corresponding to a transition to the quiescent state of the burst cycle. Finally, the lack of spiking activity causes E_K to decay back to a baseline level as the trajectory of the neuron travels back to the saddle-node bifurcation curve, where it re-enters the spiking regime of the burst. Hence, the dynamical system yields parabolic bursting behavior that terminates in a homoclinic bifurcation.

In classic parabolic bursting, burst initiation occurs when the trajectory induced by the dynamics of the slow subsystem, which includes two or more slow variables, crosses a SNIC bifurcation curve for the fast subsystem. As fast spikes ensue, the trajectory of the averaged slow equations eventually progresses back across the SNIC curve, terminating the active phase of the burst. Thus, the spikes near both burst onset and burst termination are slower than those in the heart of the burst, resulting in a parabolic dependence of spike frequency on spike number within the burst (Rinzel, 1987). This paper adds to the collection of past works that have included variations on this structure, including crossings of additional fast subsystem bifurcation curves during the active phase, which result in corresponding variability of burst profiles

(Rubin et al., 2009; Barreto & Cressman, 2011; Rubin et al., 2018). Specifically, due to the interplay of dynamic E_K and I_{NaP}, the ramping bursts in our model terminate via a crossing of a homoclinic bifurcation curve for the fast subsystem, rather than a SNIC, with little slowing of spiking at the end of the burst. In theory, a homoclinic crossing should also be associated with some spike slowing, but the quantitative details are system-specific (Rubin et al., 2018). Future work to extend this model to take into account dynamics of other ion concentrations, in addition to $[K^+]$, may yield even more diverse burst profiles (cf. Barreto and Cressman, 2011). Specifically, in addition to Na^+ dynamics, the dynamics of Cl^- is an often-overlooked factor that could contribute to ramping bursts (Currin et al., 2020; Pace et al., 2007). Importantly, concentrations of ions that impact neuronal dynamics can be coupled through pumps that transport multiple ion types, so modeling the details of this dynamics in the context of neuronal bursting represents an interesting challenge for future work.

Analysis of model robustness revealed multiple insights. The exact values of $\left(\bar{g}_{NaP}, \bar{g}_L\right)$ where bursting occurs in this model differ from the experimental data presented in (Del Negro et al., 2002; Purvis et al., 2007) and include a narrower range of $\bar{g}_L$ for each fixed $\bar{g}_{NaP}$. The difference relative to the modeling work in Purvis et al. (2007) makes sense as that study used the model of I_{NaP}-based bursting proposed in (Butera et al., 1999), which incorporates a different membrane capacitance compared to our model. Moreover, the experiments for which k_{bath} was reported were performed at elevated k_{bath} (Del Negro et al., 2002), which would tend to expand the bursting region to larger $\bar{g}_L$. In comparison to previous models of pre-BötC neuron dynamics, the model proposed in this paper exhibits similar robustness with respect to variations in parameters, while offering a greater degree of modulation of burst geometry characteristics, such as frequency, duration, and duty cycle. One exception is that our model's bursting behavior does not extend over the full range of $\bar{g}_L/C$ over which bursting occurs in the model by Butera et al. (1999). However, robustness of pre-BötC bursting to $\bar{g}_L/C$ has not been experimentally tested. Experiments suggest that the ratio $\bar{g}_{NaP}/\bar{g}_L$ is what determines whether bursting occurs, rather than the maximal leakage conductance itself (Del Negro et al., 2001, 2002; Purvis et al., 2007) (cf. the nearly linear boundaries of the bursting regions in our Figs. 5 and 6). While our decision to treat E_L as a constant allowed us to compare our model directly to earlier ones where leak strength was used to explore model behavior, E_L may in reality be nonlinearly modulated by ion dynamics (Koizumi & Smith, 2008; Huang et al., 2015). The robustness of bursting that we found with respect to variations in $\bar{g}_L$ supports the claim that the ramping dynamics that we have studied will persist with the inclusion of E_L dependence on dynamic ion concentrations, but incorporating this effect in the model and tuning it appropriately is beyond the scope of the current study. Another future direction will be the inclusion of additional membrane currents, such as I_A, I_{KCa}, the Ca^{2+}-activated nonspecific cation (CAN) current, and the Na/K pump current, which have been shown to have a significant effect on pre-BötC neuron and network dynamics in multiple past experimental and computational works (Hayes et al., 2008; Pace et al., 2007; Zavala-Tecuapetla et al., 2008; Krey et al., 2010; Jasinski et al., 2013; Koizumi et al., 2018; Picardo et al., 2019; Rubin et al., 2009; Dunmyre et al., 2011; Phillips et al., 2018, 2019).

The results of this study reveal a potential role of dynamic ion concentrations in producing and shaping ramping behavior within neuronal bursting. Previous computational studies of pre-BötC neuron activity have ignored the dynamics of $[K^+]_{out}$, modeling it as a fixed parameter. This viewpoint has been utilized in experimental studies as well, where $[K^+]_{out}$ has often been viewed as equivalent to the potassium concentration of the solution used to bathe slices of neural tissue during experimentation (k_{bath}). Our study implies that the physiologically observed oscillations of $[K^+]_{out}$ can have a significant impact on pre-BötC neuron dynamics; moreover, similar effects could emerge in prolonged bursting behavior of other neurons and should be incorporated in corresponding models in future work. Rather than assuming that $k_{bath} = [K^+]_{out}$, our model incorporates k_{bath} as an environmental factor that can affect the dynamics of $[K^+]_{out}$ via diffusion, following the framework of previous computational models that considered dynamic ion concentrations (Barreto & Cressman, 2011). The role of k_{bath} is important because k_{bath} can be modulated experimentally, providing a way for the mechanism proposed in this paper to be tested. If $[K^+]_{out}$ governs ramping dynamics through the mechanism proposed in this paper, then it would be expected that increasing k_{bath} would cause a much faster build-up of $[K^+]_{out}$, translating to a faster increase in spiking frequency throughout the burst and hence a steeper frequency ramp. Adjusting k_{bath} to lie above some level would remove the ramping effect all together, as $[K^+]_{out}$ buildup would primarily be driven by the excess influx of external potassium from the bathing solution, rather than the export of internal potassium during spiking. Similarly, lowering k_{bath} should correspond to slowing the rise in frequency over the course of the burst. Setting k_{bath} below some threshold would cause the rate of removal of $[K^+]_{out}$ via diffusion to increase enough to entirely prevent the $[K^+]_{out}$ buildup needed to induce a bursting state. It is our hope that future experiments will consider the effects of potassium concentration in the bathing solution on the dynamic ramping behavior of individual neurons, to test the mechanisms proposed in this paper. A complication, however, is that prolonged changes in k_{bath} may induce other compensatory effects (Okada et al., 2005; Ransdell et al., 2012; He et al., 2020).

Another important future research direction related to this work should involve an expansion of the scope of the model, specifically to analyze the effects of ion-dependent ramping on the generation and control of respiratory rhythms. The intrinsic dynamic mechanisms within individual neurons and synaptic network interactions work together to generate and modulate breathing rhythms (e.g., Molkov et al. (2017); Del Negro et al. (2018); Rubin and Smith (2019); Phillips and Rubin (2019); Phillips et al. (2019)), together with feedback pathways and other control signals that integrate breathing with other behaviors (as modeled, for example, in Ben-Tal and Smith (2008); Molkov et al. (2014); Diekman et al. (2017)). A specific first step to link these factors would be to construct a computational network of both pacemaker and non-pacemaker neurons in the pre-BötC and to model the effects of ramping behavior in pacemakers on the recruitment of non-pacemakers, to advance our understanding of the generation and patterning of inspiratory neural bursts (Kam et al. 2013; Kallurkar et al., 2020). A potential approach to the network modeling problem would be to address the inherent limitations of using a system of ODEs in depicting neuronal behavior. Spatial interactions, which can be an important factor in network dynamics, are not captured by ODE models. This is especially relevant for our model as it incorporates diffusion, a naturally spatially-dependent process, to differentiate between the equilibrium concentration of external potassium (k_{bath}) and localized concentration of potassium near the neuronal membrane ($[K^+]_{out}$). Hence, one possible research direction would be the development of a network-based model that utilizes both ODEs and PDEs to depict the spiking behavior of individual neurons and spatially dependent processes governing ion dynamics, respectively. The development of the PDE component of the model would have to incorporate $[K^+]_{out}$ as both a space- and time-dependent variable, which allows the spiking behavior of each neuron to affect the localized external ion concentrations of its neighboring neuron and is subject to the boundary conditions imposed by the presence of the bathing solution (e.g., a Dirichlet boundary condition forcing $[K^+]_{out}$ to take a value of k_{bath} at the boundaries of a modeled brain slice).

To summarize, this paper presents a new model of neuronal bursting in pacemaker neurons, which results in a frequency ramp at bursting onset. This effect was demonstrated to be a manifestation of parabolic bursting dynamics that allows for a broad range of burst frequencies and duty cycles. The results of this study imply that oscillations in external potassium concentration can play a significant role in the ramping dynamics of pre-BötC neurons. This ion-dependent ramping mechanism should be tested in future experimental studies and incorporated in future models of networks of pre-BötC neurons, and is likely relevant to prolonged bursting dynamics in other neurons and neuronal populations.

Appendix 1

Constants and parameters

The complete list of parameters used for this model is shown below. Certain parameters were fixed for all simulations, while others were varied for different tests. These instances will be noted.

Universal & Experimental Constants:

- Elementary Charge: $q = 1.602 \times 10^{-19}\ C$.
- Avogadro Constant: $N_A = 6.022 \times 10^{23}\ \frac{1}{mol}$.
- Unit Time Constant: $\tau = 1000\ \frac{ms}{s}$.
- Ratio of Volumes: $\beta = 14.555$ (modified from Barreto and Cressman (2011), $\beta = 7$).
- Membrane Capacitance: $C = 36$ pF (taken from Rybak et al. (2007)).

Derived Constants:

- Current Conversion Constant: $\gamma = 7.214 \times 10^{-3}\ \frac{mM}{s \cdot pA}$ (derived in Appendix 2).

Maximal Conductances:

- $\bar{g}_{Na} = 150$ nS (taken from Jasinski et al. (2013)).
- $\bar{g}_{NaP} = 5$ nS (taken from Bacak et al. (2016b)). Varied as parameter in Sect. 4.
- $\bar{g}_K = 160$ nS (taken from Jasinski et al. (2013)).
- $\bar{g}_L = 2.5$ nS (taken from Jasinski et al. (2013), $\bar{g}_L \in [2, 3]$). Varied as parameter in Sect. 4.
- $\bar{g}_{Syn} = 0.365$ nS. (Introduced in this paper to represent constant synaptic drive, in contrast to model in Bacak et al. (2016b) where $\bar{g}_{Syn} = 0$). Varied as parameter in Sect. 4.

Ion Concentrations & Reversal Potentials:

- $[Na^+]_{out} = 120$ mM (taken from Jasinski et al. (2013)).
- $[Na^+]_{in} = 15$ mM (taken from Izhikevich (2007), $[Na^+]_{in} \in [5, 15]$ mM).
- $E_{Na} = 26.7 \cdot \log \frac{[Na^+]_{out}}{[Na^+]_{in}} = 55.5$ mV. (Consistent with Rybak et al. (2007), $E_{Na} = 55$ mV).
- $[K^+]_{in} = 160$ mM (modified from Izhikevich (2007); Jasinski et al. (2013), $[K^+]_{in} = 140$ mM).
- $E_L = -68$ mV (taken from Jasinski et al. (2013)).
- $E_{Syn} = -10$ mV (taken from Jasinski et al. (2013)).

Parameters for Fast Sodium (I_{Na}) and Persistent Sodium (I_{NaP}):

- $V_{m_{Na}} = -43.8$ mV, $k_{m_{Na}} = 6$ mV, $V_{\tau_{m_{Na}}} = -43.8$ mV, $k_{\tau_{m_{Na}}} = 14$ mV.
- $V_{h_{Na}} = -67.5$ mV, $k_{h_{Na}} = -11.8mV$, $V_{\tau_{h_{Na}}} = -67.5$ mV, $k_{\tau_{h_{Na}}} = -12.8$ mV.
- $V_{m_{NaP}} = -47.1$ mV, $k_{m_{NaP}} = 3.1$ mV, $V_{\tau_{m_{NaP}}} = -47.1$ mV, $k_{\tau_{m_{NaP}}} = 6.2$ mV.
- $V_{h_{NaP}} = -60$ mV, $k_{h_{NaP}} = -9$ mV, $V_{\tau_{h_{NaP}}} = -60$ mV, $k_{\tau_{h_{NaP}}} = 9$ mV.
- $\bar{\tau}_{m_{Na}} = 0.25$ mS, $\bar{\tau}_{h_{Na}} = 8.46$ mS, $\bar{\tau}_{m_{NaP}} = 1$ mS, $\bar{\tau}_{h_{NaP}} = 5000$ mS.
- All of these parameters were taken directly from Bacak et al. (2016a), with the exception of $k_{h_{Na}}$, which was altered from a value of -10.8 mV to the listed value of -11.8 mV.

Parameters for Delayed Rectifier Potassium Current (I_K):

- $n_A = 0.01\,\frac{1}{mV}$, $n_{A_V} = 44$ mV, $n_{A_k} = 5$ mV, $n_B = 0.17$, $n_{B_V} = 49$ mV, $n_{B_k} = 40$ mV.
- All values taken from Bacak et al. (2016b).

Parameters for Diffusion of Extracellular Potassium ($[K^+]_{out}$):

- $k_{bath} = 4$ mM (taken from Barreto and Cressman (2011)).
- $\tau_{diff} = 750$ mS (numerically equivalent to the formulation in Barreto and Cressman (2011), which uses $\frac{1}{\tau_{diff}} \equiv \frac{\epsilon}{\tau}$, where $\epsilon = 1.333$ Hz and $\tau = 1000\frac{\text{mS}}{\text{s}}$).

Parameters for Glia:

- $\bar{G} = 10\frac{mM}{s}$, $\bar{K} = 5mM$, $z_K = 6\frac{1}{mM}$.
- These parameter values were altered from those in Barreto and Cressman (2011). In Barreto and Cressman (2011), the concentration of $[K^+]_{out}$ remains far below the mid-point value of the sigmoidal function in Eq. (10). The parameters were adjusted such that the range of dynamic $[K^+]_{out}$ was distributed over the midpoint of Eq. (10), ensuring that the nonlinear behavior of glial cells was represented.

Appendix 2

Derivation of γ

Our initial assumption is that the neuron is roughly spherical, or rather that the majority of the cell's volume is contained in a sphere. From Barreto and Cressman (2011), the radius of the neuron is taken to be approximately $r = 7.0\ \mu$m. Hence, the internal volume of the neuron can be approximated as $V_{in} = \frac{4}{3}\pi r^3 = 1.44 \times 10^{-9}$ mL.

The internal concentration c_{in} can be determined from the total number of ions N, the internal volume V_{in}, and Avogadro's Constant N_A:

$$c_{in} = N \cdot \frac{1}{N_A} \cdot \frac{1}{V_{in}}.$$

Note that the ions we are measuring concentrations of are Na^+ and K^+, both of which have a $+1$ charge. Letting $q = 1.60 \times 10^{-19}$ C, we can express the concentration in terms of total charge, Q:

$$c_{in} = \frac{N}{V_{in}N_A} \cdot \frac{q}{q} = \frac{Q}{qV_{in}N_A}.$$

Differentiating, we get:

$$\frac{dc_{in}}{dt} = \frac{d}{dt}\left(\frac{Q}{qV_{in}N_A}\right) = \frac{dQ}{dt} \cdot \frac{1}{qV_{in}N_A} = I \cdot \frac{1}{qV_{in}N_A}.$$

By taking the ratio of this expression to the current, we can determine:

$$\gamma \equiv \frac{1}{qV_{in}N_A} = 7.2 \times 10^3 \frac{\text{mol}}{\text{C} \cdot \text{mL}}.$$

By the following dimensional analysis manipulation, we obtain:

$$\frac{\text{mol}}{\text{C} \cdot \text{mL}} \cdot \left(10^3 \frac{\text{mmol}}{\text{mol}} \cdot 10^3 \frac{\text{mL}}{\text{L}} \cdot \frac{\text{mM} \cdot \text{L}}{\text{mmol}} \cdot \frac{\text{C}}{\text{A} \cdot \text{s}} \cdot 10^{-12} \frac{\text{A}}{\text{pA}} \cdot 10^{-3} \frac{\text{s}}{\text{ms}}\right) = 10^{-9} \frac{\text{mM}}{\text{ms} \cdot \text{pA}}.$$

Thus, we conclude:

$$\gamma = 7.214 \times 10^{-6}\ \frac{\text{mM}}{\text{ms}} \cdot \frac{1}{\text{pA}}. \tag{12}$$

Appendix 3

A closer look at transitions in behavior as E_K is varied

As illustrated in Fig. 1, if the K^+ concentration is held fixed, then shifting the E_K value has a clear effect on the long-term periodic behavior of the model neuron. Each periodic behavior, whether tonic spiking or bursting, can be depicted as a stable limit cycle projected to the (h_{NaP}, V) phase space. As shown in Fig. 3, with increases in E_K, the stable oscillation switches from tonic spiking to bursting, and then, with additional increases, from bursting back to spiking. Which behavior arises depends on whether the periodic orbit family of the fast subsystem terminates in a SNIC bifurcation or a homoclinic bifurcation and on where this termination lies relative to the h_{NaP} nullcline.

Here we construct a bifurcation diagram to present in more detail the changes in stable periodic behavior that occur with E_K as a bifurcation parameter. More specifically, when the neuronal system exhibits bursting, each burst is composed of a finite number of action potentials, each associated with an approximately constant V, h_{NaP}. Therefore, for each fixed h_{NaP}, we identify the corresponding periodic spiking or bursting attractor and record the h_{NaP} value at which each spike occurs within this attractor (Fig. 8).

In this bifurcation diagram, each dot denotes the value of h_{NaP} at which an action potential occurs during 80 seconds of simulated bursting behavior, for a corresponding fixed value of E_K. For each E_K, the spikes from the first 55 seconds of neuron simulation are not shown, such that the diagram omits the transient state and only reflects the attractors of the system. For sufficiently low E_K, the stable dynamics consists of periodic tonic spiking, characterized by a single h_{NaP} value for each E_K in the diagram. As E_K increases, the transition from a tonic spiking state to a bursting state appears to arise through a chaotic period doubling mechanism (Fig. 8A,B), estimated numerically to occur just above $E_K = -91.2$ mV.

The transition from bursting back to tonic spiking, depicted in Fig. 8A,C, is less clear cut. The spike branch at highest h_{NaP} values seems to disappear instantly as E_K increases. We expect that this change is related to the phenomena shown in Figs. 1C, 3D. In the solution displayed in Fig. 1C, it appears that bursting is about to begin, but instead a plateau of depolarization block occurs. From Fig. 3D, we can appreciate that the AH point has moved to smaller h_{NaP} than that of the fold point, such that the trajectory's initial jump to the active phase does not yield a full spike. Only after h_{NaP} drifts to lower values, below the AH point, can spiking ensue. With an additional increase in E_K to just below -83.1 mV, most of the remaining spike branches disappear together, leaving only a cluster of values near $h_{NaP} = 0.155$. We also notice pockets of variability in h_{NaP} as E_K varies between -83.4 and

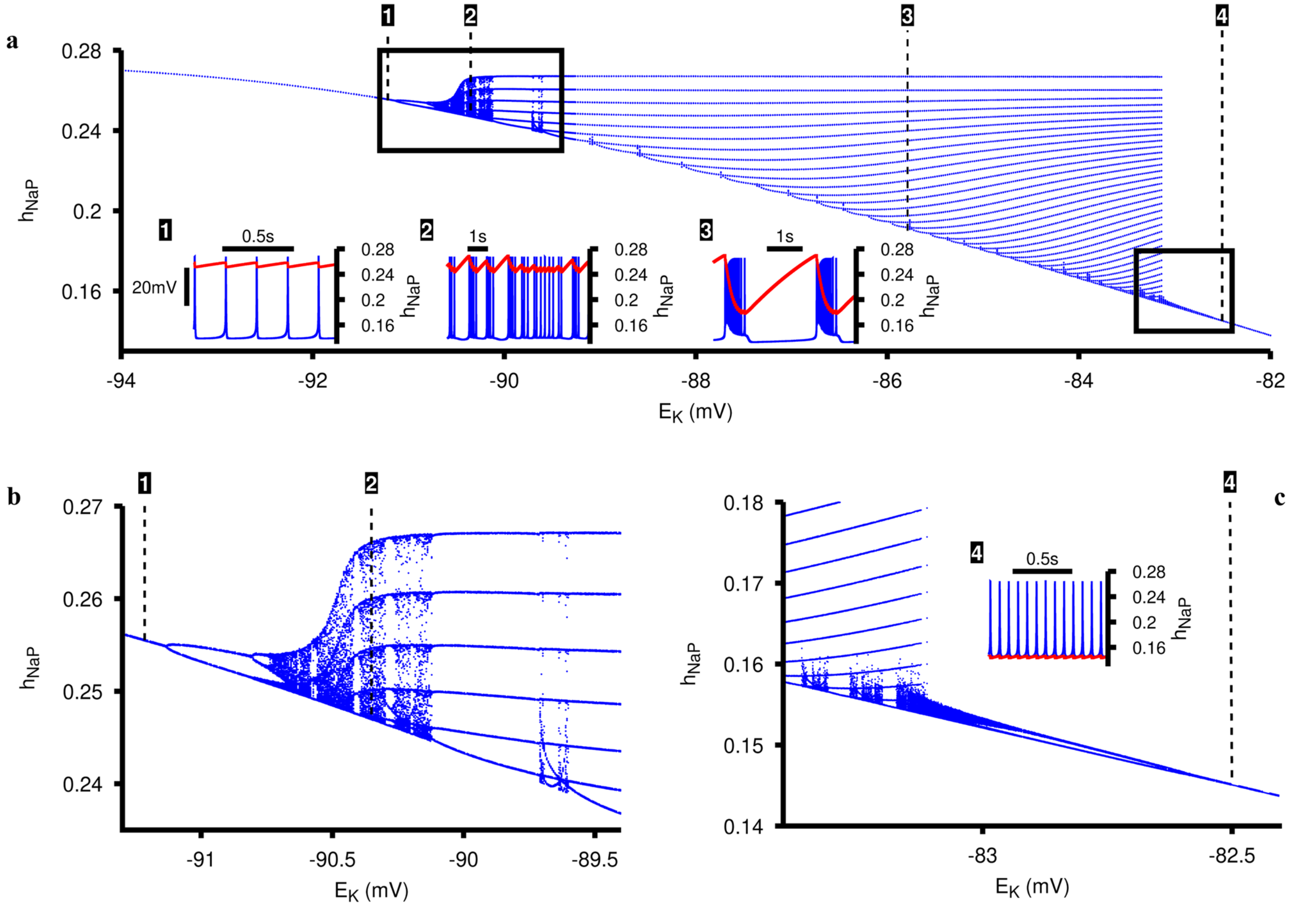

Fig. 8 Bifurcation diagram of attracting dynamics of the neuronal model with $[K^+]_{out}$ (and hence E_K) used as the bifurcation parameter, varied in steps of 0.001 mV. (**A**) Bifurcation diagram over the entire bursting interval. Each blue dot represents an h_{NaP} value on a single spike within the attractor for the corresponding E_K. Insets show voltage and h_{NaP} time courses at the fixed values of E_K marked by the numbered vertical dashed lines on the diagram. (**B**-**C**) Zoomed views of different parts of the diagram in (**A**)

−83.1 mV. Interestingly, inspection of the voltage trace suggests that periodic spiking begins at about $E_K = -82.6$ mV, above the value at which most of the collection of h_{NaP} branches disappears.

Elucidating the details of this bifurcation is beyond the scope of our consideration of ramping bursts in the full model and remains for future inquiry, which would require more detailed simulations and analysis.

Appendix 4

1-fast-2-slow Analysis

The dynamics of ramping bursts can be understood through a fast-slow decomposition analysis. The first step was the fast-slow decomposition analysis discussed in Sect. 3.2. As shown in Fig. 3, this analysis involved fixing $[K^+]_{out}$ and determining the geometry that governs the model trajectory in the $\left(V, h_{NaP}\right)$-phase space. This analysis can naturally be extended into a three-dimensional fast-slow decomposition by including $[K^+]_{out}$, or equivalently E_K, as a second slow variable. The various important geometric objects identified with fixed $[K^+]_{out}$ values, namely critical manifolds, fast subsystem saddle-node and Andronov-Hopf (AH) bifurcation points, and corresponding fast subsystem periodic orbits become higher dimensional surfaces and curves when projected to the $\left(V, h_{NaP}, E_K\right)$-phase space. For instance, the individual AH points become an AH curve, and the periodic orbits initiated there form a smooth manifold originating from this curve. A visualization of this three-dimensional structure is illustrated in Fig. 9, along with the superimposed trajectory of a neuron with dynamic $[K^+]_{out}$ exhibiting ramping bursts.

The period during which spiking occurs or active phase of the burst occurs where the trajectory oscillates between the prongs of the green periodic orbit manifold in Fig. 9. As discussed in Sect. 3.3, this oscillation drives build-up of $[K^+]_{out}$, moving the trajectory in the direction of increasing E_K. This potassium ion build-up causes an increase in spiking frequency within the burst, facilitating further external potassium accumulation through a positive feedback loop. This process continues until the trajectory reaches a point along the homoclinic curve where the periodic orbit family terminates and returns to the hyperpolarized stable component of the critical manifold. This corresponds to the quiescent phase of the burst, where the trajectory remains until it reaches the saddle-node curve where it returns to the active phase. Additional insight arises from visualizing the local minima and maxima that occur throughout the active phase of the burst. In Fig. 10 these local extrema are connected into two curves. Clearly, the trajectory of the neuron travels along the family of periodic orbits during the burst, moving away from and back towards the homoclinic curve as time advances and E_K increases. Furthermore, the neuron experiences a decline in spike amplitude when it pulls away from the edge of the periodic orbit family where it starts and terminates.

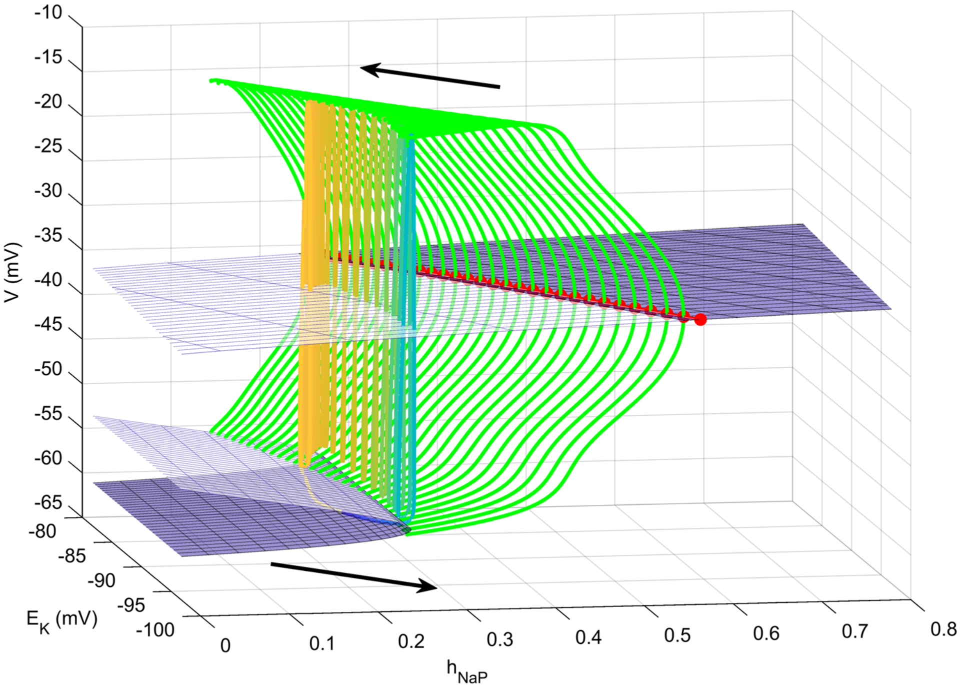

Fig. 9 The periodic trajectory of the ramping burst solution in (V, h_{NaP}, E_K)-space is color coded temporally, progressing in time from blue to yellow. Additionally, the two black arrows indicate the direction that the trajectory travels. The upper and lower blue surfaces represent stable components of the critical manifold; white/blue surfaces between these are unstable components, which meet in a saddle-node curve at negative h_{NaP} (not shown). Also shown are the AH curve (red) and the surfaces of maximal and minimal V along the family of periodic orbits originating at the AH curve (green)

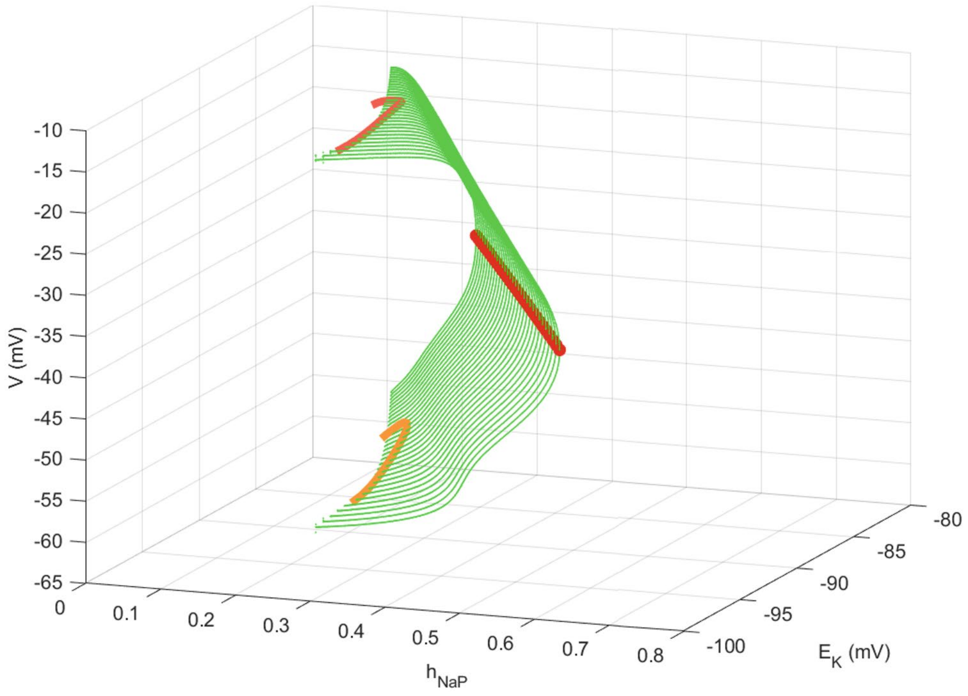

Fig. 10 Once again, the red curve indicates fast subsystem AH points and the green manifold consists of extremal voltages of periodic orbits emanating from the AH curve. Superimposed on this manifold are traces of minimum (lower, orange) and maximum (upper, red-orange) values of voltage attained for each spike within the burst, connected into smooth curves

Acknowledgements The authors would like to acknowledge the Program in Neural Computation at the Center for the Neural Basis of Cognition for their help in facilitating this research collaboration

Funding This work was partially supported by NSF awards DMS-1612913 and DMS-1950195 to JER. Additional funding was provided by the University of Florida through the Wentworth Travel Scholarship and the University Scholars Program.

Data availability Not applicable.

Code availibility The XPP and MATLAB codes used in this work will be uploaded to ModelDB, where they will be freely available, upon acceptance of this work for publication.

Declarations

Conflicts of interest The authors have no conflicts of interest to disclose.

References

Amzica, F., Massimini, M., & Manfridi, A. (2002). Spatial buffering during slow and paroxysmal sleep oscillations in cortical networks of glial cells in vivo. *Journal of Neuroscience, 22*(3), 1042–1053. https://doi.org/10.1523/JNEUROSCI.22-03-01042.2002

Bacak, B. J., Kim, T., Smith, J. C., Rubin, J. E., & Rybak, I. A. (2016a). Mixed-mode oscillations and population bursting in the pre-Bötzinger complex. *eLife* 5:e13403. https://doi.org/10.7554/eLife.13403

Bacak, B. J., Segaran, J., & Molkov, Y. (2016b). Modeling the effects of extracellular potassium on bursting properties in pre-Bötzinger complex neurons. *Journal of Computational Neuroscience, 40*(2), 231–245. https://doi.org/10.1007/s10827-016-0594-8

Barreto, E., & Cressman J. R. (2011). Ion concentration dynamics as a mechanism for neuronal bursting. *Journal of Biological Physics, 37*(3), 361–373. https://doi.org/10.1007/s10867-010-9212-6

Baylor, D. A., & Nicholls, J. G. (1969). Changes in extracellular potassium concentration roduced by neuronal activity in the central nervous system of the leech. *Journal of Physiology, 203*(3), 555–569. https://doi.org/10.1016/0166-2236(96)10040-0

Beckner, M. E. (2020). A roadmap for potassium buffering/dispersion via the glial network of the CNS. *Neurochemistry international, 136*, 104727. https://doi.org/10.1016/j.neuint.2020.104727

Ben-Tal, A., & Smith, J. C. (2008). A model for control of breathing in mammals: coupling neural dynamics to peripheral gas exchange and transport. *Journal of Theoretical Biology, 251*(3), 480–497. https://doi.org/10.1016/10.1016/j.jtbi.2007.12.018

Bertram, R., & Rubin, J. E. (2017). Multi-timescale systems and fast-slow analysis. *Mathematical Biosciences, 287*, 105–121. https://doi.org/10.1016/j.mbs.2016.07.003

Butera, R. J., Rinzel, J., & Smith, J. C. (1999). Models of respiratory rhythm generation in the pre-Bötzinger complex. I. Bursting pacemaker neurons. *Journal of Neurophysiology, 82*(1), 382–397. https://doi.org/10.1152/jn.1999.82.1.382

Chevalier, M., Toporikova, N., Simmers, J., & Thoby-Brisson, M. (2016). Development of pacemaker properties and rhythmogenic mechanisms in the mouse embryonic respiratory network. *elife* 5:e16125. https://doi.org/10.7554/eLife.16125

Clausen, M. V., Hilbers, F., & Poulsen, H. (2017). The structure and function of the Na, K-ATPase isoforms in health and disease. *Frontiers in Physiology, 8*, 371. https://doi.org/10.3389/fphys.2017.00371

Currin, C. B., Trevelyan, A. J., Akerman, C. J., & Raimondo, J. V. (2020). Chloride dynamics alter the input-output properties of neurons. *PLoS Computational Biology, 16*(5), e1007932. https://doi.org/10.1371/journal.pcbi.1007932

Del Negro, C. A., Johnson, S. M., Butera, R. J., & Smith, J. C. (2001). Models of respiratory rhythm generation in the pre-Bötzinger complex. III. Experimental tests of model predictions. *Journal of Neurophysiology, 86*(1), 59–74. https://doi.org/10.1152/jn.2001.86.1.59

Del Negro, C. A., Koshiya, N., Butera, R. J., & Smith, J. C. (2002). Persistent sodium current, membrane properties and bursting behavior of pre-Bötzinger complex inspiratory neurons in vitro. *Journal of Neurophysiology, 88*(5), 2242–2250. https://doi.org/10.1152/jn.00081.2002

Del Negro, C. A., Morgado-Valle, C., Hayes, J. A., Mackay, D. D., Pace, R. W., Crowder, E. A., & Feldman, J. L. (2005). Sodium and calcium current-mediated pacemaker neurons and respiratory rhythm generation. *Journal of Neuroscience, 25*(2), 446–453. https://doi.org/10.1523/JNEUROSCI.2237-04.2005

Del Negro, C. A., Funk, G. D., & Feldman, J. L. (2018). Breathing matters. *Nature Reviews Neuroscience, 19*(6), 351–367. https://doi.org/10.1038/s41583-018-0003-6

Diekman, C. O., Thomas, P. J., & Wilson, C. G. (2017). Eupnea, tachypnea, and autoresuscitation in a closed-loop respiratory control model. *Journal of Neurophysiology, 118*(4), 2194–2215. https://doi.org/10.1152/jn.00170.2017

Dunmyre, J. R., Del Negro, C. A., & Rubin, J. E. (2011). Interactions of persistent sodium and calcium-activated nonspecific cationic currents yield dynamically distinct bursting regimes in a model of respiratory neurons. *Journal of Computational Neuroscience, 31*(2), 305–328. https://doi.org/10.1007/s10827-010-0311-y

Erhardt, A. H., Mardal, K. A., & Schreiner, J. E. (2020) Dynamics of a neuron–glia system: the occurrence of seizures and the influence of electroconvulsive stimuli: A mathematical and numerical study. *Journal of Computational Neuroscience, 48*(2), 229–251. https://doi.org/10.1007/s10827-020-00746-5

Ermentrout, B. (2002). Simulating, Analyzing, and Animating Dynamical Systems: A Guide To Xppaut for Researchers and Students. Society for Industrial and Applied Mathematics, USA.

Ermentrout, G. B., & Kopell, N. (1986). Parabolic bursting in an excitable system coupled with a slow oscillation. *SIAM Journal on Applied Mathematics, 46*(2), 233–253. https://doi.org/10.1137/0146017

Ezure, K., Tanaka, I., & Saito, Y. (2003). Activity of brainstem respiratory neurones just before the expiration?inspiration transition in the rat. *Journal of Physiology, 547*(2), 629–640. https://doi.org/10.1113/jphysiol.2002.032805

Fröhlich, F., Bazhenov, M., Iragui-Madoz, V., & Sejnowski, T. J. (2008). Potassium dynamics in the epileptic cortex: new insights on an old topic. *Neuroscientist, 14*(5), 422–433. https://doi.org/10.1177/1073858408317955

Gray, P. A., Rekling, J. C., Bocchiaro, C. M., & Feldman, J. L. (1999). Modulation of respiratory frequency by peptidergic input to rhythmogenic neurons in the preBötzinger complex. *Science, 286*(5444), 1566–1568. https://doi.org/10.1126/science.286.5444.1566

Hayes, J. A., Mendenhall, J. L., Brush, B. R., & Del Negro, C. A. (2008). 4-Aminopyridine-sensitive outward currents in preBötzinger complex neurons influence respiratory rhythm generation in neonatal mice. *Journal of Physiology, 586*(7), 1921–1936. https://doi.org/10.1113/jphysiol.2008.150946

He, L. S., Rue, M. C., Morozova, E. O., Powell, D. J., James, E. J., Kar, M., & Marder, E. (2020). Rapid adaptation to elevated extracellular potassium in the pyloric circuit of the crab, Cancer borealis. *Journal of Neurophysiology, 123*(5), 2075–2089. https://doi.org/10.1152/jn.00135.2020

Hodgkin, A., & Huxley, A. (1952). A quantitative description of membrane current and its application to conduction and excitation in nerve. *Journal of Physiology, 117*(4), 500–544. https://doi.org/10.1113/jphysiol.1952.sp004764

Huang, S., Hong, S., & De Schutter, E. (2015). Non-linear leak currents affect mammalian neuron physiology. *Frontiers in Cellular Neuroscience, 9*(432), 1–10. https://doi.org/10.3389/fncel.2015.00432

Huguenard, J. R., & McCormick, D. A. (1992). Simulation of the currents involved in rhythmic oscillations in thalamic relay neurons. *Journal of Neurophysiology, 68*(4), 1373–1383. https://doi.org/10.1152/jn.1992.68.4.1373

Izhikevich, E. M. (2007) Dynamical Systems in Neuroscience: The Geometry of Excitability and Bursting. Massachusetts Institute of Technology, Cambridge, MA.

Jasinski, P. E., Molkov, Y. I., Shetsova, N. A., Smith, J. C., & Rybak, I. A. (2013). Sodium and calcium mechanisms of rhythmic bursting in excitatory neural networks of the pre-Bštzinger complex: a computational modelling study.*European Journal of Neuroscience, 37*(2), 212–230. https://doi.org/10.1111/ejn.12042

Johnson, S. M., Smith, J. C., Funk, G. D., & Feldman, J. L. (1994). Pacemaker behavior of respiratory neurons in medullary slices from neonatal rat. *Journal of Neurophysiology, 72*(6), 2598–2608. https://doi.org/10.1152/jn.1994.72.6.2598

Kallurkar, P. S., Grover, C., Picardo, M. C. D., & Del Negro, C. A. (2020). Evaluating the burstlet theory of inspiratory rhythm and pattern generation. *eNeuro, 7*(1), 1–12. https://doi.org/doi.org/10.1523/ENEURO.0314-19.2019

Kam, K., Worrell, J. W., Janczewski, W. A., Cui, Y., & Feldman, J. L. (2013). Distinct inspiratory rhythm and pattern generating mechanisms in the preBötzinger complex. *Journal of Neuroscience, 33*(22), 9235–9245. https://doi.org/10.1523/JNEUROSCI.4143-12.2013

Kofuji, P., & Newman, E. A. (2004). Potassium buffering in the central nervous system. *Neuroscience, 129*(4), 1043–1054. https://doi.org/10.1016/j.neuroscience.2004.06.008

Shella Keilholz Koizumi, H., & Smith, J. C. (2008). Persistent Na^+ and K^+- dominated leak currents contribute to respiratory rhythm generation in the pre-Bötzinger complex in vitro. *Journal of Neuroscience, 28*(7), 1773–1785. https://doi.org/10.1523/JNEUROSCI.3916-07.2008

Koizumi, H., Smerin, S. E., Yamanishi, T., Moorjani, B. R., Zhang, R., & Smith, J. C. (2010). TASK channels contribute to the K^+-dominated leak current regulating respiratory rhythm generation in vitro. *Journal of Neuroscience, 30*(12), 4273–4284. https://doi.org/10.1523/JNEUROSCI.4017-09.2010

Koizumi, H., John, T. T., Chia, J. X., Tariq, M. F., Phillips, R. S., Mosher, B., Chen, Y., Thompson, R., Zhang, R., Koshiya. N., & Smith, J. C. (2018). Transient receptor potential channels TRPM4 and TRPC3 critically contribute to respiratory motor pattern formation but not rhythmogenesis in rodent brainstem circuits. *eNeuro, 5*(1), 1–22. https://doi.org/10.1523/ENEURO.0332-17.2018

Krey, R. A., Goodreau, A. M., Arnold, T. B., & Del Negro, C. A. (2010). Outward currents contributing to inspiratory burst termination in preBötzinger Complex neurons of neonatal mice studied in vitro. *Frontiers in Neural Circuits, 4*(124), 1–9. https://doi.org/10.3389/fncir.2010.00124

Kueh, D., Barnett, W. H., Cymbalyuk, G. S., & Calabrese, R. L. (2016). Na^+/K^+ pump interacts with the h-current to control bursting activity in central pattern generator neurons of leeches. *eLife* 5:e19322. https://doi.org/10.7554/eLife.19322

Lindsey, B. G., Rybak, I. A., & Smith, J. C. (2012). Computational models and emergent properties of respiratory neural networks. *Comprehensive Physiology, 2*(3), 1619–1670. https://doi.org/10.1002/cphy.c110016

Molkov, Y. I., Shevtsova, N. A., Park, C., Ben-Tal, A., Smith. J. C., Rubin, J. E., & Rybak, I. A. (2014). A closed-loop model of the respiratory system: focus on hypercapnia and active expiration. *PloS One, 9*(10), e109894. https://doi.org/10.1371/journal.pone.0109894

Molkov, Y. I., Rubin, J. E., Rybak, I. A., & Smith, J. C. (2017). Computational models of the neural control of breathing. *Wiley Interdisciplinary Reviews: Systems Biology and Medicine, 9*(2). https://doi.org/10.1002/wsbm.1371

Newman, E., & Reichenbach, A. (1996). The Müller cell: a functional element of the retina. *Trends in Neurosciences, 19*(8), 307–312. https://doi.org/10.1016/0166-2236(96)10040-0

Nicholson, C., & Syková. E. (1998). Extracellular space structure revealed by diffusion analysis. *Trends in Neurosciences, 21*(5), 207–215. https://doi.org/10.1016/s0166-2236(98)01261-2

Okada, Y., Kuwana, S., Kawai, A., Mückenhoff, K., & Scheid, P. (2005). Significance of extracellular potassium in central respiratory control studied in the isolated brainstem–spinal cord preparation of the neonatal rat. *Respiratory Physiology & Neurobiology, 146*(1), 21–32. https://doi.org/10.1016/j.resp.2004.10.009

Pace, R. W., Mackay, D. D., Feldman, J. L., & Del Negro, C. A. (2007). Inspiratory bursts in the preBötzinger complex depend on a calcium–activated non–specific cation current linked to glutamate receptors in neonatal mice. *Journal of Physiology, 582*(1), 113–125. https://doi.org/10.1113/jphysiol.2007.133660

Peña, F., Parkis, M. A., Tryba, A. K., & Ramirez, J. M. (2004). Differential contribution of pacemaker properties to the generation of respiratory rhythms during normoxia and hypoxia. *Neuron, 43*(1), 105–117. https://doi.org/10.1016/j.neuron.2004.06.023

Phillips, R. S., & Rubin, J. E. (2019). Effects of persistent sodium current blockade in respiratory circuits depend on the pharmacological mechanism of action and network dynamics. *PLoS Computational Biology, 15*(8), e1006938. https://doi.org/10.1371/journal.pcbi.1006938

Phillips, R. S., John, T. T., Koizumi, H., Molkov, Y. I., & Smith, J. C. (2019). Biophysical mechanisms in the mammalian respiratory oscillator re-examined with a new data-driven computational model. *eLife* 8:e41555. https://doi.org/10.7554/eLife.41555

Phillips, W. S., Del Negro, C. A., & Rekling, J. C. (2018). Dendritic A-current in rhythmically active preBötzinger complex neurons in organotypic cultures from newborn mice. *Journal of Neuroscience, 38*(12), 3039–3049. https://doi.org/10.1523/JNEUROSCI.3342-17.2018

Picardo, M. C. D., Sugimura, Y. K., Dorst, K. E., Kallurkar, P. S., Akins, V. T., Ma, X., Teruyama, R., Guinamard, R., Kam, K., Saha, M. S., & Del Negro, C. A. (2019). TRPM4 ion channels in pre-Bötzinger complex interneurons are essential for breathing motor pattern but not rhythm. *PLoS Biology, 17*(2), e2006094. https://doi.org/10.1371/journal.pbio.2006094

Purvis, L. K., Smith, J. C., Koizumu, H., & Butera, R. J. (2007). Intrinsic bursters increase the robustness of rhythm generation in an excitatory network. *Journal of Neurophysiology, 97*(2), 1515–1526. https://doi.org/10.1152/jn.00908.2006

Raimondo, J. V., Burman, R. J., Katz, A. A., & Akerman, C. J. (2015). Ion dynamics during seizures. *Frontiers in Cellular Neuroscience, 9*(419), 1–14. https://doi.org/10.3389/fncel.2015.00419

Ransdell, J. L., Nair, S. S., & Schulz, D. J. (2012). Rapid homeostatic plasticity of intrinsic excitability in a central pattern generator network stabilizes functional neural network output. *Journal of Neuroscience, 32*(28), 9649–9658. https://doi.org/10.1523/JNEUROSCI.1945-12.2012

Rekling, J. C., & Feldman, J. L. (1998). PreBötzinger complex and pacemaker neurons: hypothesized site and kernel for respiratory rhythm generation. *Annual Review of Physiology, 60*(1), 385–405. https://doi.org/10.1146/annurev.physiol.60.1.385

Richter, D. W. (1996). Neural regulation of respiration: rhythmogenesis and afferent control. In R. Greger, & U. Windhorst (Eds.), Comprehensive human physiology (pp. 2079–2095). Springer, Berlin, Heidelberg.

Rinzel, J. (1987). A formal classification of bursting mechanisms in excitable systems. In E. Teramoto, & M. Yamoguti (Eds.), Mathematical topics in population biology, morphogenesis and neurosciences (pp. 267–281), Springer-Verlag, New York, NY.

Rubin, J. E., Krauskopf, B., & Osinga, H. (2018). Natural extension of fast–slow decomposition for dynamical systems. *Physical Review E, 97*(1), 012215. https://doi.org/10.1103/PhysRevE.97.012215

Rubin, J. E., & Smith, J. C. (2019). Robustness of respiratory rhythm generation across dynamic regimes. *PLoS Computational Biology, 15*(7), e1006860. https://doi.org/10.1371/journal.pcbi.1006860

Rubin, J. E., Hayes, J. A., Mendenhall. J. L., & Del Negro, C. A. (2009) Calcium-activated nonspecific cation current and synaptic depression promote dependent burst oscillators. *Proceedings of the National Academy of Sciences, 106*(8), 2939–2944. https://doi.org/10.1073/pnas.0808776106

Rubin, J. E., Shevtsova, N. A., Ermentrout, G. B., Smith, J. C., & Rybak, I. A. (2009). Multiple rhythmic states in a model of the respiratory central pattern generator. *Journal of Neurophysiology, 101*(4), 2146–2165. https://doi.org/10.1152/jn.90958.2008

Rybak, I. A., Abdala, A. P. L., Markin, S. N., Paton, J. F. R., & Smith, J. C. (2007). Spatial organization and state-dependent mechanisms for respiratory rhythm and pattern generation. *Progress in Brain Research, 165*, 201–220. https://doi.org/10.1016/S0079-6123(06)65013-9

Smith, J. C., Ellenberger, H. H., Ballanyi, K., Richter, D. W., & Feldman, J. L. (1991). Pre-Bötzinger complex: a brainstem region that may generate respiratory rhythm in mammals. *Science, 254*(5032), 726–729. https://doi.org/10.1126/science.1683005

Somjen, G. G. (2004) Ions in the Brain: Normal Function, Seizures, and Stroke. Oxford University Press, New York, NY.

Teka, W., Tabak, J., & Bertram, R. (2012). The relationship between two fast/slow analysis techniques for bursting oscillations. *Chaos: An Interdisciplinary Journal of Nonlinear Science, 22*(4), 043117. https://doi.org/10.1063/1.4766943

Thoby-Brisson, M., & Ramirez, J. M. (2001). Identification of two types of inspiratory pacemaker neurons in the isolated respiratory neural network of mice. *Journal of Neurophysiology, 86*(1), 104–112. https://doi.org/10.1152/jn.2001.86.1.104

Toporikova, N., Chevalier, M., & Thoby-Brisson, M. (2015). Sigh and eupnea rhythmogenesis involve distinct interconnected subpopulations: a combined computational and experimental study. *eNeuro, 2*(2), 1–18. https://doi.org/10.1523/ENEURO.0074-14.2015

Tryba, A. K., Peña, F., & Ramirez, J. M. (2003). Stabilization of bursting in respiratory pacemaker neurons. *Journal of Neuroscience, 23*(8), 3538–3546. https://doi.org/10.1523/JNEUROSCI.23-08-03538.2003

Vo, T., Tabak, J., Bertram, R., & Wechselberger, M. (2014). A geometric understanding of how fast activating potassium channels promote bursting in pituitary cells. *Journal of Computational Neuroscience, 36*(2), 259–278. https://doi.org/10.1007/s10827-013-0470-8

Wang, J., Lu, B., Liu, S., & Jiang, X. (2017). Bursting types and bifurcation analysis in the pre-Bötzinger complex respiratory rhythm neuron. *International Journal of Bifurcation and Chaos, 27*(1), 1750010. https://doi.org/10.1142/S0218127417500109

Wang, Y., & Rubin, J. E. (2016). Multiple timescale mixed bursting dynamics in a respiratory neuron model. *Journal of Computational Neuroscience, 41*(3), 245–268. https://doi.org/10.1016/j.mbs.2016.07.003

Wang, Y., & Rubin, J. E. (2020). Complex bursting dynamics in an embryonic respiratory neuron model. *Chaos: An Interdisciplinary Journal of Nonlinear Science, 30*(4), 043127. https://doi.org/10.1063/1.5138993

Zavala-Tecuapetla, C., Aguileta, M., Lopez-Guerrero, J., González-Marín, M., & Peña, F. (2008). Calcium-activated potassium currents differentially modulate respiratory rhythm generation. *European Journal of Neuroscience, 27*(11), 2871–2884. https://doi.org/10.1111/j.1460-9568.2008.06214.x